

Review

# Recent Progress and Challenges in Controlling Secondary Phases in Kesterite CZT(S/Se) Thin Films: A Critical Review

Mohamed Yassine Zaki  and Alin Velea \* 

National Institute of Materials Physics, Atomistilor 405A, 077125 Magurele, Romania; yassine.zaki@infim.ro

\* Correspondence: alin.velea@infim.ro

**Abstract:** Kesterite-based copper zinc tin sulfide (CZTS) and copper zinc tin selenide (CZTSe) thin films have attracted considerable attention as promising materials for sustainable and cost-effective thin-film solar cells. However, the successful integration of these materials into photovoltaic devices is hindered by the coexistence of secondary phases, which can significantly affect device performance and stability. This review article provides a comprehensive overview of recent progress and challenges in controlling secondary phases in kesterite CZTS and CZTSe thin films. Drawing from relevant studies, we discuss state-of-the-art strategies and techniques employed to mitigate the formation of secondary phases. These include a range of deposition methods, such as electrodeposition, sol-gel, spray pyrolysis, evaporation, pulsed laser deposition, and sputtering, each presenting distinct benefits in enhancing phase purity. This study highlights the importance of employing various characterization techniques, such as X-ray diffraction, Raman spectroscopy, scanning electron microscopy, and energy-dispersive X-ray spectroscopy, for the precise identification of secondary phases in CZTS and CZTSe thin films. Furthermore, the review discusses innovative strategies and techniques aimed at mitigating the occurrence of secondary phases, including process optimization, compositional tuning, and post-deposition treatments. These approaches offer promising avenues for enhancing the purity and performance of kesterite-based thin-film solar cells. Challenges and open questions in this field are addressed, and potential future research directions are proposed. By comprehensively analyzing recent advancements, this review contributes to a deeper understanding of secondary phase-related issues in kesterite CZT(S/Se) thin films, paving the way for enhanced performance and commercial viability of thin-film solar cell technologies.



**Citation:** Zaki, M.Y.; Velea, A. Recent Progress and Challenges in Controlling Secondary Phases in Kesterite CZT(S/Se) Thin Films: A Critical Review. *Energies* **2024**, *17*, 1600. <https://doi.org/10.3390/en17071600>

Academic Editor: Elisa Artegiani

Received: 25 February 2024

Revised: 24 March 2024

Accepted: 25 March 2024

Published: 27 March 2024



**Copyright:** © 2024 by the authors. Licensee MDPI, Basel, Switzerland. This article is an open access article distributed under the terms and conditions of the Creative Commons Attribution (CC BY) license (<https://creativecommons.org/licenses/by/4.0/>).

**Keywords:** kesterite solar cells; CZTS; CZTSe; secondary phases

## 1. Introduction

The kesterite family comprises copper zinc tin sulfide (CZTS), copper zinc tin selenide (CZTSe), and their sulfoselenide variant, copper zinc tin sulfoselenide (CZTSSe). These compounds belong to the class of quaternary semiconductors and share a kesterite crystal structure. CZTS, CZTSe, and CZTSSe have drawn considerable interest in the realm of solar energy due to their abundance, non-toxicity, and promising optical and electronic characteristics [1]. CZTS, the sulfide counterpart, is composed of copper (Cu), zinc (Zn), tin (Sn), and sulfur (S). On the other hand, CZTSe substitutes selenium (Se) for sulfur, resulting in a selenide compound. CZTSSe, as the name suggests, is a combination of both sulfur and selenium [2]. These compounds have been explored for their potential in thin-film solar cells, offering a sustainable alternative to conventional materials [3]. The direct bandgap of these materials falls within the optimal range for solar absorption, approximately 1.0–1.5 eV [4]. This aligns with the solar spectrum, allowing for efficient conversion of sunlight into electricity. Additionally, the high absorption coefficient and high extinction coefficient of kesterite make them promising for the development of thin-film solar cells with a low thickness requirement [5]. However, achieving high performance

kesterite solar cells is still challenging due to the narrow phase stability of the quaternary phase, the formation of secondary phases, and the presence of defects [6].

Despite their promise, challenges such as phase stability, the formation of secondary phases, and the presence of defects are obstacles in achieving high-performance solar cells [7]. Various vacuum and non-vacuum deposition techniques have been explored to synthesize CZTS and CZTSe thin films [8], such as evaporation, pulsed laser deposition, magnetron sputtering, electrodeposition, sol-gel, and spray pyrolysis. However, different deposition techniques and conditions can result in differences in the properties of the films, such as phase purity, composition, morphology, and electronic properties [9]. This review will focus on the synthesis methods of copper zinc tin sulfide (CZTS) and copper zinc tin selenide (CZTSe), emphasizing key techniques to obtain single-phase films. Moreover, this review aims to provide a comprehensive understanding of the impact of secondary phases on the performance and stability of kesterite-based solar devices. By analyzing the challenges associated with secondary phase occurrence, this study aims to identify effective strategies for mitigating their formation and enhancing the efficiency of CZTS and CZTSe thin-film solar cells. Additionally, we will explore the role of various deposition techniques in controlling phase purity and discuss the importance of precise characterization methods for identifying and quantifying secondary phases. This concise review aims to offer insights into optimizing CZTS and CZTSe absorber layers for enhanced solar cell applications.

## 2. Deposition Techniques

Regarding CZT(S/Se) growth, diverse synthesis approaches have been employed for depositing these absorber layers. In the more prevalent two-step fabrication techniques, the initial phase involves the preparation of the Cu, Zn and Sn (CZT) metal precursor. This precursor is then subjected to a sulfurization or selenization, followed annealing treatment, ultimately leading to the formation of CZT(S/Se) by reaction of the elements. On the other hand, one-step methods simplify the process by directly producing CZT(S/Se) in a single step, which is subsequently refined through heat treatment. The efficacy of the resulting solar cell device depends on critical factors such as the deposition rate, layer thickness, and the specific synthesis method employed. Achieving optimal performance requires a detailed understanding of these parameters, and the continuous exploration of synthesis strategies.

### 2.1. Solution-Based Approaches

#### 2.1.1. Electrodeposition

The electrodeposition technique has emerged as a versatile and promising approach for the synthesis of high-quality  $\text{Cu}_2\text{ZnSnS}_4$  (CZTS) and  $\text{Cu}_2\text{ZnSnSe}_4$  (CZTSe) thin films in solar cell applications. The process includes a three-electrode cell, consisting of a working electrode (commonly a substrate on which deposition occurs), a counter electrode, and a reference electrode. The working electrode is usually coated with a precursor solution containing copper, zinc, tin, and sulfur or selenium sources. The electrochemical cell is immersed in this precursor solution. A power supply is employed to apply a controlled potential or current between the working and counter electrodes, facilitating the deposition onto the working electrode. The reference electrode monitors the electrochemical potential as sketched in Figure 1.

In recent years, electrochemical deposition techniques have gained importance as cost-effective and environmentally friendly methods for depositing large-area thin films. These techniques encompass both single-step and sequential electrodeposition approaches. In the single-step method, all constituents are sourced from a single electrolyte, while in sequential electrodeposition, different metal salts are sequentially deposited and annealed to form the final film. Electrodeposition offers precise control over film composition and thickness. Numerous studies have investigated the electrodeposition process, focusing on optimizing various parameters to achieve desired film properties. One important aspect is the composition of the electrolyte solution, where precise control over the concentration

ratios of the metal ions to be electrodeposited is essential. Hreid et al. demonstrated that adjusting these concentrations influences the stoichiometry and phase purity of deposited CZTSe films [10]. Another important parameter is the deposition potential, which modulates the rate of electrodeposition and thereby influences the crystal structure and phase composition of the films. Azmi et al. explored this aspect by varying the deposition potential to tune the electrochemical reduction in metal ions, they revealed that adequate potential for CZTS phase electrodeposition is  $-1.1$  V [11]. Furthermore, deposition time plays an important role in determining film thickness, morphology and composition as shown by Valdes et al. [12]. They have concluded that a CZTSe absorber deposited in 10 min lead to the best performing solar cell, and increasing in deposition time decreases device performance. The pH of the electrolyte solution also influences the ionization state of metal ions during electrodeposition. Variations in pH can impact the chemical composition, morphology, and crystallinity of the deposited films, maintaining a  $\text{pH} = 4.8$  is optimal for achieving high-quality CZTS absorber layers [13]. The role of additives, particularly complexing agents, should also be taken into account. These agents form stable complexes with metal ions, influencing deposition processes. Their inclusion has been explored to enhance uniformity, to control grain size, and to modulate crystallinity. The choice of a specific complexing agent, or combinations of different agents, and their concentration plays a role in tailoring the electrodeposition process [14–17] for fine-tuning film properties. Additionally, stirring or agitation during electrodeposition ensures uniform ion distribution in the electrolyte solution, contributing to enhanced film quality and uniformity [17].

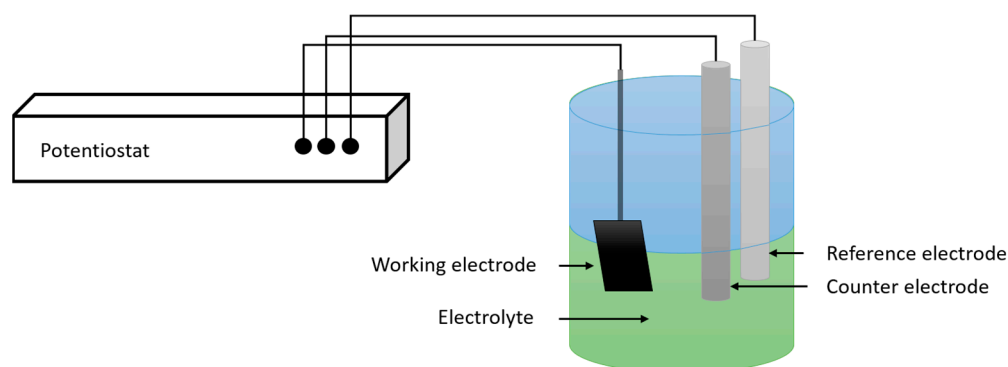


**Figure 1.** Electrodeposition technique schematic for CZT(S/Se) thin films deposition.

### 2.1.2. Sol-Gel

The sol-gel deposition method is a cost-effective and relatively simple technique for synthesizing CZT(S/Se) thin films. The process can be carried out in two steps, starting with the preparation of an aqueous solution containing the sol-gel precursors, followed by spin coating the solution onto the substrate to obtain the desired deposits as presented in Figure 2. This technique is well-developed in the thin film industry due to its reproducibility for large-scale fabrication. However, despite its advantages, very few studies have been conducted on the synthesis of CZT(S/Se) thin films using sol-gel deposition.

The synthesis of CZTS and CZTSe thin films involves a meticulous exploration of several critical parameters, each influencing the properties of the resulting films. The precursor composition determines the elemental ratios and, consequently, the stoichiometry of the compound. Variations in the precursors concentrations in the solution have been studied to understand their impact on film composition. In a study conducted by Amrit et al., sol-gel CZTS thin films were prepared without sulfurization. They investigated the influence of precursor concentration on the properties of the films. Their findings revealed that optimal concentrations resulted in well-defined kesterite phase formation, uniform film surfaces, and variations in optical bandgap [18]. The substrate temperature is influencing crystallinity, grain size, and structural properties. Khushaim et al., have explored the effects of different deposition temperatures on the properties of CZTS films,

and have found that a substrate temperature of 350 °C is ideal for obtaining adequate properties [19]. Preheating annealing is a common practice to enhance crystallinity and phase purity, and the variation in different environments, as explored by Ahmoum et al., demonstrating that CZTS films preheated in Ar and N<sub>2</sub> exhibit enhanced crystallinity, larger grains, uniform surface morphology and optimal elemental composition [20]. Furthermore, additives and complexing agents in the precursor solution can influence nucleation and growth as demonstrated by Chaudhari et al., can influence nucleation and growth [21]. Post-deposition annealing is commonly employed to enhance the crystallinity and phase purity of CZTS and CZTSe films. The annealing conditions, including temperature and duration, can significantly impact the structural and optoelectronic properties of the films. Ahmed et al. investigated the effect of annealing temperatures on CZTS compounds [22]. They revealed that annealing at 450 °C results in high crystalline films, with a decrease in optical band gap to 1.6 eV and improved electrical conductivity. On the other hand, Shaikh et al., studied the impact of annealing time on the properties of CZTS films, and demonstrated that longer annealing times leads to improvements in conductivity, light absorption, and mechanical stability [23].

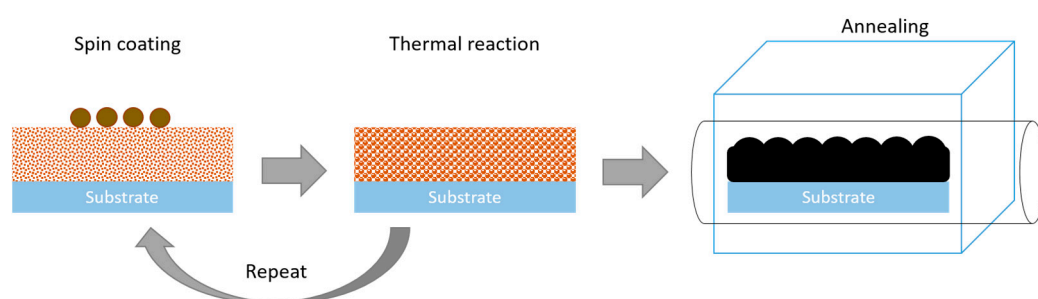


**Figure 2.** Sol-gel schematic process for thin film deposition.

### 2.1.3. Spray Pyrolysis

Spray pyrolysis deposition is a widely used technique in thin film production due to its easy process and relatively simple manipulation. This method, thanks to its simplicity and reproducibility, is well-known for its application in large-scale synthesis of thin film semiconductors. One of the most significant advantages of this technique is that it does not require any vacuum steps throughout the process, making it suitable for industrial commercial production. Spray pyrolysis involves atomizing a precursor solution onto a heated substrate. The equipment includes a substrate holder, spray nozzle, heater, and gas delivery system (Figure 3).

Spray pyrolysis stands as a versatile method for CZTS thin film synthesis, offering a multitude of adjustable parameters that influence the resulting film properties. Among these parameters, substrate temperature holds significance, dictating crystallinity and grain size development [24]. Additionally, precursor concentration serves as a critical factor, impacting film thickness and elemental composition [25]. The pH of the solution can also have an influence the different properties of the obtained CZTS films as stated by Kumar et al. [26]. Furthermore, the choice of annealing conditions post-deposition is important in determining the final film structure and properties [27]. Kamoun et al. shown that variations in spray duration influences the resulting CZTS films, with the film having the most adequate properties being obtained at an annealing temperature of 550 °C in 10 min [28].

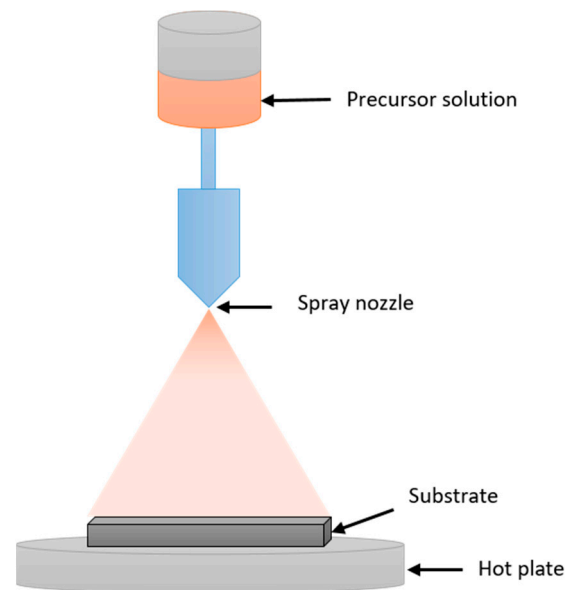


**Figure 3.** Sketch of Spray pyrolysis deposition method.

## 2.2. Physical-Based Approaches

### 2.2.1. Evaporation

Evaporation techniques have been widely employed by researchers for depositing CZT(S/Se) absorber layers. The development of these layers through various evaporation technologies such as electron beam evaporation, co-evaporation, rapid thermal evaporation, and thermal evaporation has led to the fabrication of high-quality absorber materials. Evaporation methods are straightforward in principle and enable the production of films with excellent quality. However, controlling the stoichiometry of the elements is challenging [29], resulting in lower cell efficiency. Additionally, the vacuum-based deposition process wastes source materials, leading to relatively high costs.

This technique utilizes a vacuum chamber and an evaporation source, typically a heated crucible. In this process, the material is vaporized and deposited onto a substrate placed strategically within the vacuum environment. The substrate may have controlled movement for uniform film deposition (Figure 4). The deposition of CZT(S/Se) films by evaporation can be achieved through two different approaches: single-step deposition [30,31], where all the precursors are simultaneously deposited and then followed by sulfurization, and sequential two-step deposition using different metallic or binary precursors, in different combinations and sequences, such as Cu/Sn/Zn/Cu, Cu/Sn/Cu/Zn [32], Cu-ZnS-Sn [33] or CuSn/Zn/Se/CuSn/Se [34], followed by annealing with a sulfur or selenium source.

### 2.2.2. Pulsed Laser Deposition

Pulsed Laser Deposition (PLD) remains one of the best methods for producing high-quality CZT(S/Se) thin films with complex compositions. This technique is known for its numerous advantages, such as its simplicity and process flexibility, improved crystallinity, and the ability to obtain clean films owing to the absence of atmospheric gases. The PLD comprises a laser system, target material, vacuum chamber, and a substrate holder. A high-energy laser vaporizes the target, creating a plume that deposits onto a substrate in the vacuum chamber (Figure 5). PLD systems manage deposition rate, temperature, and pressure, often incorporating in situ monitoring tools for real-time analysis. However, the literature shows limited work conducted using this method, despite its significant advantages for CZT(S/Se) thin film deposition.

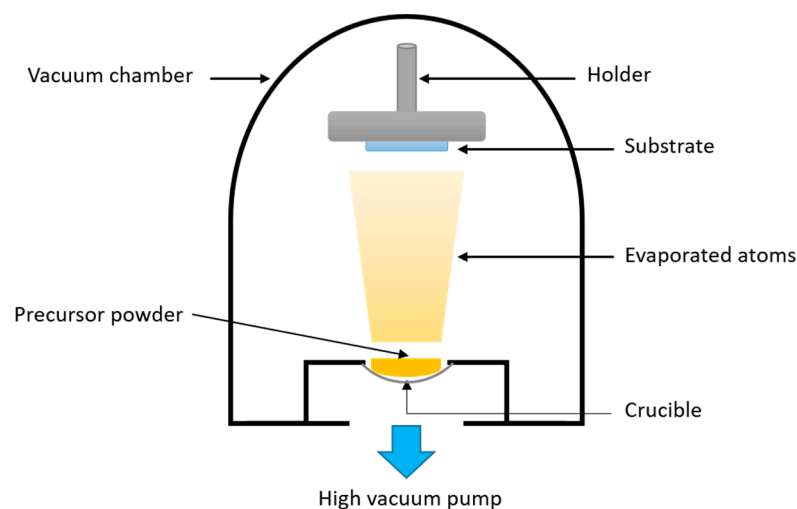


**Figure 4.** Evaporation schematic setup for CZT(S/Se) films synthesis.

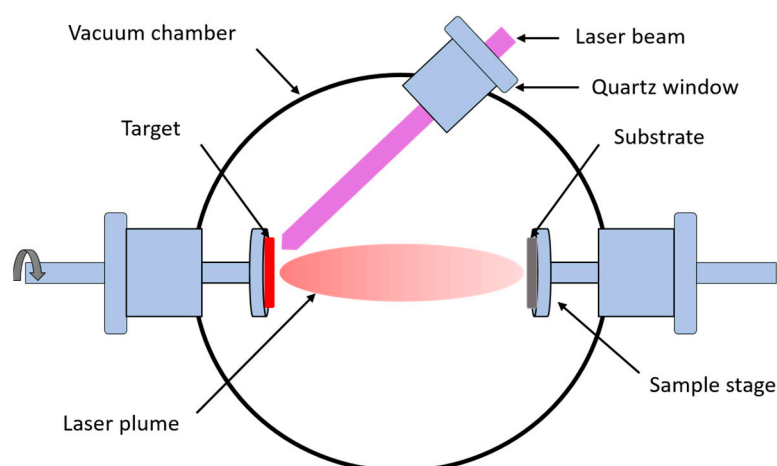


**Figure 5.** Schematic of a classical Pulsed Laser Deposition technique.

PLD can be used for depositing thin films on diverse substrates, offering versatility [35]. Recognized for its high deposition rate and quality film growth facilitated by high-energy processes [36], PLD presents a convenient method for CZTS film synthesis. This can occur in a one-step process by employing a CZTS target and a heated substrates at elevated temperatures, or in a two-step process involving the deposition of metallic (Cu, Zn, and Sn) films followed by sulfurization [37]. Key parameters, including the substrate-to-target distance, substrate orientation and temperature, laser energy, and target composition, influence film properties. The choice of metallic targets allows control over layer thickness and roughness, while a single CZTS target, comprising is preferred for achieving stoichiometric  $\text{Cu}_2\text{ZnSnS}_4$  materials [38]. Despite its advantages, PLD encounters challenges such as droplet formation leading to unwanted phases and inhomogeneity, especially when using multiple crystalline phase targets. Drawbacks include extended processing times for large film thicknesses and challenges in producing extensive area films [39,40].

### 2.2.3. Magnetron Sputtering

Sputtering is a widely used fabrication method offering uniformity and reproducibility in large-scale production, particularly in solar cell manufacturing. Magnetron sputtering system is a physical vapor deposition technique widely used for producing thin films with excellent uniformity. This system employs a magnetron—a high-powered magnet that enhances the sputtering process (Figure 6). Key parameters like pressure, power, and deposition time can be adjusted for optimal film quality and desired properties. However,

challenges such as the loss of tin during high-temperature post-deposition treatment and the formation of secondary phases need to be addressed.

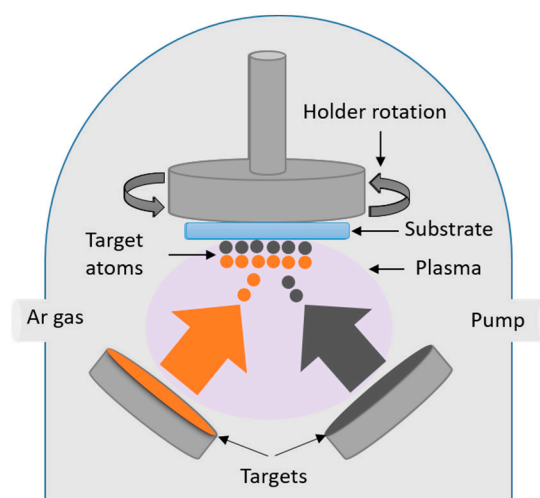


**Figure 6.** Schematic diagram of Magnetron sputtering deposition method.

Magnetron sputtering is renowned for its ability to synthesize thin films on extensive substrates [41]. In CZTS synthesis, the system allows for substrate heating during deposition or sulfurization after sputtering [42,43]. It supports diverse targets, including metallic precursors, binary sulfide targets, or single quaternary targets [44]. The choice of direct current (DC) sputtering for elemental conductive targets (Cu, Zn, Sn) and radio frequency (RF) for binary and quaternary targets ensures efficient deposition [45,46]. Magnetron sputtering provides control over chemical composition, film thickness, uniformity, adhesion, and substrate coverage, achieving high deposition rates and purity [47,48]. Challenges such as target poisoning and cracking at high power need consideration [49,50].

### 3. Secondary Phases in CZT(S/Se)

#### 3.1. Formation of Secondary Phases

The formation of secondary phases stands out as a significant challenge in the growth of CZTS and CZTSe absorber layers. Its primary source is the off-stoichiometric composition in the CZT(S/Se) films [51,52]. Various factors such as the decomposition of the CZT(S/Se) at high temperatures [53], variations in precursor deposition methods [54], or the sulfurization/selenization treatment parameters [55] influences the formation of secondary phases. While there are various secondary phases that can appear within the CZTS or CZTSe films, in this review we will focus on the most frequently occurring phases in the two compounds. Binary alloys like  $\text{Cu}_x(\text{S/Se})$ ,  $\text{Zn}(\text{S/Se})$ ,  $\text{Sn}_x(\text{S/Se})_y$ ,  $\text{Mo}(\text{S/Se})_x$  or ternary compositions such as  $\text{Cu-Sn-(S/Se)}$  are the most common phases to form during CZT(S/Se) film growth. The delicate balance of precursor ratios and an overabundance of the Cu, Zn, Sn and S/Se elements can influence the composition, introducing unwanted phases and affecting the properties of the absorber layer.

The formation of copper-based phases such as  $\text{CuS}$  and  $\text{Cu}_2\text{S}$  is common under excess of copper conditions [56]. Cu-rich environment can lead to increased doping of CZTS, proving harmful to solar cells. For this reason, the current focus is on growing CZTS with a Cu-poor and Zn-rich composition. Moreover, the excess in zinc might contribute to the appearance of zinc sulfide ( $\text{ZnS}$ ) [57]. This phase is highly observed at both the front and back interfaces within the CZTS compound. The impact of  $\text{ZnS}$  phase was found to be detrimental to the solar device, especially on the surface of CZTS. Further, tin sulfide compounds ( $\text{Sn}_x\text{S}_y$ ) and their impact on CZTS solar cells have been less explored. The formation of the  $\text{SnS}$ ,  $\text{SnS}_2$  and  $\text{Sn}_2\text{S}_3$  phases is due to the presence of a surplus of tin in the development of CZTS [58,59].  $\text{Sn}_x\text{S}_y$  can be detected on both the surface and back of

the CZTS film. Additionally, the emergence of MoS<sub>2</sub> can be attributed to the reaction of the molybdenum back contact with sulfur, presenting another facet of secondary phase formation influenced by the synthesis environment. In the case of Cu<sub>x</sub>Sn<sub>y</sub>S<sub>z</sub> compounds such as Cu<sub>2</sub>SnS<sub>3</sub> (CTS), which the most frequent secondary phase in CZTS films, the apparition of these phases is due to several reasons such as low zinc content, incomplete reaction at low temperature during film growth, or the decomposition of the CZTS at high temperature.

Similarly, in the context CZTSe thin films, secondary phases may arise due to the same factors. Binary phases such as Cu<sub>x</sub>Se, Sn<sub>x</sub>Se<sub>y</sub>, ZnSe and MoSe<sub>2</sub> may form as a consequence of the reaction of Se with the related elements if they are in excess [60], while the case of Cu<sub>x</sub>Sn<sub>y</sub>Se<sub>z</sub> and mainly the Cu<sub>2</sub>SnSe<sub>3</sub> (CTSe) phase is resembling its homologue CTS. Similar to CZTS, the balance of precursor ratios plays a role in determining the composition and subsequent phase evolution in CZTSe films.

Understanding and controlling the deposition parameters and chemical reactions are essential for minimizing the presence of unwanted secondary phases, thereby optimizing the structural and electronic properties of CZT(S/Se) absorber layers for enhanced photovoltaic performance. Additionally, consideration of annealing treatments becomes imperative in managing secondary phase formation, adding another layer of complexity to the fabrication process.

### 3.2. Identification of Secondary Phases

The characterization of secondary phases in CZTS and CZTSe thin films leads to the understanding the structural and compositional properties. Several main characterization techniques are employed for this purpose. X-ray diffraction (XRD) is a fundamental technique that helps identify the crystalline phases present in the films by analyzing their diffraction patterns. Raman spectroscopy is employed to study vibrational modes, providing insights into the chemical composition and crystal structure. Scanning electron microscopy (SEM) and transmission electron microscopy (TEM) are essential for visualizing the microstructure and morphology, aiding in the identification of secondary phases. Energy-dispersive X-ray spectroscopy (EDS) coupled with SEM or TEM provides elemental composition information, aiding in mapping the distribution of elements and phases within the films. X-ray photoelectron spectroscopy (XPS) is valuable for determining the chemical states of elements and detecting surface composition variations. These techniques collectively offer a comprehensive understanding of secondary phases in CZTS and CZTSe films, contributing to the optimization of their growth processes and enhancing their potential in solar cell applications. Here, we will address how some of the most used characterization techniques such as XRD, Raman, and SEM-EDX can be utilized to detect the presence of secondary phases in CZT(S/Se) films.

#### 3.2.1. Structural Analysis

##### X-ray Diffraction

X-ray diffraction (XRD) is employed to analyze the crystallographic structure of CZTS thin films and identify the presence of unwanted secondary phases. The distinctive peaks in the XRD pattern allow for the discrimination of various phases, such as Cu<sub>x</sub>S, Sn<sub>x</sub>S<sub>y</sub>, ZnS, MoS<sub>x</sub>, CTS and others, based on their unique crystal structures. Challenges may arise, particularly when secondary phases such as cubic ZnS and cubic, monoclinic or tetragonal CTS have similar crystal structures to CZTS, making their identification more complex. Despite these challenges, XRD remains a fundamental technique, providing valuable information about the composition and crystalline nature of CZTS films. Several studies have analyzed the XRD patterns of CZTS, ZnS, and CTS compounds, in order to understand the main divergences of these phases [61–63]. Berg et al. prepared CZTS, ZnS and CTS films by electrodeposition and compared the X-ray diffractograms of the different samples. They confirmed that ZnS and CTS closely resemble CZTS in their X-ray patterns. While cubic ZnS has the fewest peaks, the tetragonal CZTS phase and monoclinic ternary

phase exhibit additional minor peaks due to lower symmetry [64]. Distinguishing between CZTS, ZnS and CTS relies on identifying these minor peaks, although their absence does not conclusively exclude the presence of the respective phase, especially in the context of a textured film. In the same study, the group compared between the three phases' main peak at approximately  $2\theta = 28.5^\circ$ . They found that the angular positions of ZnS, CTS and CZTS main peaks, are differing within an angular range of  $0.2^\circ$ , suggesting the potential possibility to distinguish individual CTS and ZnS phases from the CZTS [12]. As an example of secondary phases identification relying on minor peaks, Zaki et al., prepared CZTS films by annealing in different atmospheres and for different durations sputtered ZnS layers with two thicknesses (150 and 200 nm) deposited onto a CTS layer [13]. The International Center for Diffraction Data (ICDD) were used to identify the CZTS and the coexistent secondary phases. They reported that most the peaks in the diffractograms belong to the CZTS phase, while a tiny peak at  $2\theta = 26.91^\circ$  makes it possible to identify the presence of the hexagonal ZnS phase. On the other hand, the  $\text{SnS}_2$  is easily distinguished with a peak at around  $2\theta = 50^\circ$  in the films annealed in Sn+S atmosphere, due to excess in Sn. Contrarily, the  $\text{CuS}$  ( $2\theta = 31.97^\circ$ ) phase was observed in one of the sulfurized (annealed in S only) CZTS films, due to the Sn-poor composition of the film as observed in Figure 7 [65]. The case of copper sulfides such as  $\text{CuS}$  and  $\text{Cu}_2\text{S}$  is different, since they can be easily identified through XRD, as their unique diffraction peaks ( $2\theta = 31.88^\circ$ ,  $52.58^\circ$ , and  $48.23^\circ$  for  $\text{CuS}$ ; and  $2\theta = 27.83^\circ$ ,  $32.23^\circ$ ,  $46.28^\circ$ , and  $54.78^\circ$  for  $\text{Cu}_2\text{S}$ ) significantly differ from those of CZTS. Furthermore, secondary phases like  $\text{SnS}$ ,  $\text{SnS}_2$ , and  $\text{Sn}_2\text{S}_3$  are readily detectable within CZTS films using X-ray diffraction. This detection is facilitated by the distinct diffraction patterns exhibited by these phases, which differ significantly from that of CZTS. Each secondary phase possesses characteristic diffraction peaks at specific angles as presented in Table 1, providing clear signatures for their identification. For instance,  $\text{SnS}$  typically displays intense peaks at  $2\theta$  angles of  $22.01^\circ$ ,  $26.00^\circ$ ,  $27.47^\circ$ ,  $30.47^\circ$ ,  $31.53^\circ$ ,  $31.97^\circ$ ,  $39.04^\circ$ ,  $45.49^\circ$ ,  $48.50^\circ$ ,  $51.31^\circ$ ,  $53.14^\circ$ , and  $56.67^\circ$ . Similarly,  $\text{SnS}_2$  presents distinctive peaks at  $2\theta$  angles of  $15.02^\circ$ ,  $28.19^\circ$ ,  $30.26^\circ$ ,  $32.12^\circ$ ,  $41.88^\circ$ ,  $46.12^\circ$ ,  $49.96^\circ$ , and  $52.45^\circ$ . Moreover,  $\text{Sn}_2\text{S}_3$  can be identified by its prominent peaks at  $2\theta$  angles of  $12.63^\circ$ ,  $16.10^\circ$ ,  $21.49^\circ$ ,  $23.77^\circ$ ,  $27.33^\circ$ ,  $27.68^\circ$ ,  $30.91^\circ$ ,  $32.53^\circ$ ,  $33.53^\circ$ ,  $33.79^\circ$ ,  $35.89^\circ$ ,  $36.49^\circ$ ,  $37.93^\circ$ , and  $39.85^\circ$ . These distinctive diffraction patterns enable the straightforward detection and characterization of Sn-containing secondary phases within CZTS films using XRD analysis. These last three phases are rarely observed in the CZTS system probably due to the very volatility aspect of tin.  $\text{MoS}_2$  has distinct peaks in its XRD pattern that can be differentiated from the peaks of CZTS.  $\text{MoS}_2$  typically exhibits prominent peaks at specific angles, such as  $14.4^\circ$ ,  $33.8^\circ$ ,  $39.6^\circ$ , and  $58.1^\circ$  ( $2\theta$ ), corresponding to its crystal structure. By comparing the measured XRD pattern of the CZTS film with reference patterns for  $\text{MoS}_2$ , one can identify the presence of this secondary phase.

The detection of secondary phases in CZTSe films, it is quite similar with its homologue CZTS, since CZTSe along with cubic ZnSe and cubic or monoclinic  $\text{Cu}_2\text{SnSe}_3$  (CTSe) have nearly identical XRD patterns. However, unlike  $\text{Cu}_2\text{S}$  in CZTS system, the cubic  $\text{Cu}_2\text{Se}$  also share remarkably similar structures and unit cell sizes with CZTSe [66,67]. Despite CZTSe having a tetragonal-based structure, its reflections often overlap with those of the mentioned phases due to their common cubic structures, close lattice parameters, and similar atomic scattering factors of  $\text{Cu}^+$  and  $\text{Zn}^{2+}$ . In the case of CZTSe, similar observations (as for CZTS, ZnS and CTS) can be made regarding the angular differences in main peaks compared to ZnSe and CTSe. The largest difference observed for ZnSe is  $0.15^\circ$ , while for the cubic-CTSe, it is  $0.16^\circ$  as explained by Salome et al. [68]. These slight angular variations, though relatively small, hint at the potential to distinguish between CZTSe and its constituent phases, ZnSe and CTSe. In Figure 8, are presented the diffractograms of annealed CTSe/ZnSe stacks prepared by magnetron sputtering along with the XRD patterns of the most frequent secondary phases in CZTSe films. Catana et al., synthesized in a first step CTSe films from different stacks ( $\text{Sn}\backslash\text{Cu}$ ,  $\text{SnSe}_2\backslash\text{Cu}$ ,  $\text{Sn}\backslash\text{Cu}_2\text{S}$ , and  $\text{SnSe}_2\backslash\text{Cu}_2\text{Se}$ ), then a ZnSe layer was added on top of the obtained CTSe films and the combinations were

annealed in Se atmosphere at 550 °C [69]. The identification of the ZnSe phase was almost impossible when they compared its XRD patterns to the prepared CZTSe films. While the diffraction peaks of cubic-ZnSe and cubic-CTSe overlap with those of CZTSe, each of the three phases exhibits additional tiny peaks, which can help in distinguishing between them. On the other hand, CZTSe has double peaks near 65° and 72° with a very low intensity, yet, the peaks at 53.39° and 53.53° are used for confirming the presence of CZTSe [68]. Here again, using only XRD measurements can be challenging to ascertain the existence of these phases, and the absence of the unique peaks does not definitively imply their absence. Some distinguishable phases, such as CuSe, monoclinic Cu<sub>2</sub>Se, SnSe, SnSe<sub>2</sub>, and Sn<sub>2</sub>S<sub>3</sub> can be differentiated from CZTSe in XRD due to their distinct structures and cell parameters as observed in Figure 8. The identification of secondary phases, particularly CuSe and monoclinic Cu<sub>2</sub>Se, in CZTSe using X-ray diffraction is a well-established process. The unique crystal structures of CuSe and monoclinic Cu<sub>2</sub>Se contribute to their characteristic XRD peaks at specific 2θ angles, making them easily distinguishable from the main CZTSe phase. Similarly, the detection of tin selenide secondary phases, including SnSe and SnSe<sub>2</sub>, in CZTSe is facilitated by XRD analysis. The distinctive crystal structures of these tin selenides result in characteristic diffraction patterns with well-defined peaks at specific angles. The main XRD characteristic peaks of the MoSe<sub>2</sub> phase typically include prominent peaks at 2θ around 14.4°, 33.8°, 39.6°, and 58.1°. Detecting MoSe<sub>2</sub> in CZTSe films using XRD can be both feasible and challenging. Feasibility depends on factors such as the concentration of MoSe<sub>2</sub>, film thickness, and the overall crystalline quality of the sample. If MoSe<sub>2</sub> is present in a sufficient quantity and is well crystallized, its characteristic peaks can be distinguished in the XRD pattern. However, challenges may arise if MoSe<sub>2</sub> is present in low concentrations or if the film has poor crystallinity, leading to broader or weaker diffraction peaks that might be harder to identify against the background of CZTSe peaks. In Table 2 are summarized the most intense XRD peaks of the CZTSe phase and the related recurrent secondary phases following their ICDD card number.

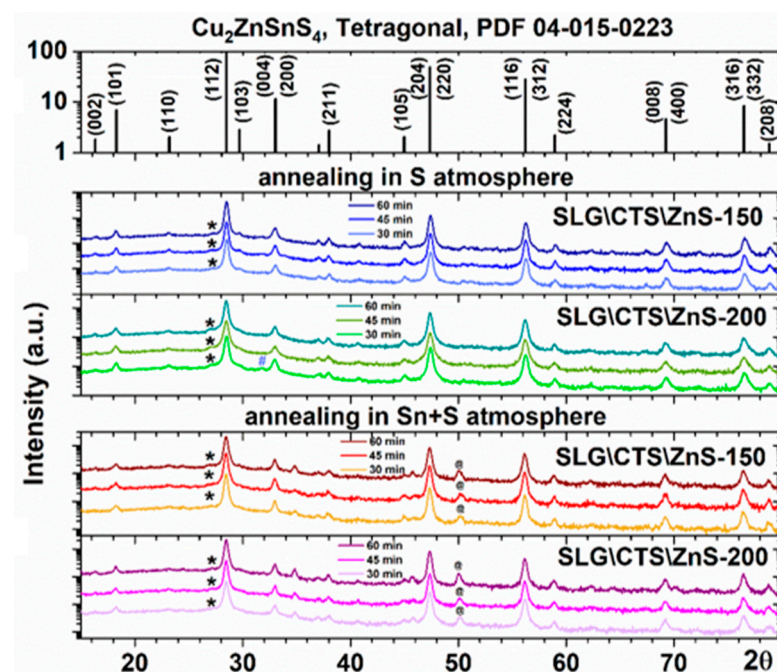


**Figure 7.** X-ray diffractograms of CZTS films obtained on ZnS layers with two different thicknesses (150 and 200 nm) deposited on top of CTS films and annealed in different atmospheres for different times. The ZnS phase (hexagonal, ICDD 04-012-8144) is indicated with “\*”, the CuS phase (hexagonal, ICDD 04-008-8460) is indicated with “#”, and the SnS<sub>2</sub> phase (hexagonal, ICDD 00-021-1231) is indicated with “@”. Reproduced with permission [65].

**Table 1.** CZTS and most frequent secondary phases XRD main peaks following their ICDD cards. The most intense peak of each phase is bolded.

Compound	Most Intense XRD Peaks (°)	ICDD Card Number
Cu <sub>2</sub> ZnSnS <sub>4</sub>	16.32, 18.24, 23.12, <b>28.44</b> , 29.64, 32.93, 36.97, 37.90, 44.94, 47.31, 56.17, 58.85, 69.08, 69.21, 76.39, 78.71	01-080-8225
Cu <sub>2</sub> SnS <sub>3</sub>	<b>28.44</b> , 32.96, 47.31, 56.13, 58.86, 69.14, 76.38, 78.75 (cubic); 16.06, 18.02, 20.88, <b>28.40</b> , 31.37, 32.89, 47.20, 56.07, 76.17 (monoclinic); <b>28.53</b> , 33.07, 47.47; 56.32, 69.38, 76.68, 79.04 (tetragonal)	01-089-2877 (cubic); 04-010-5719 (monoclinic); 04-009-7947 (tetragonal)
CuS	10.80, 27.12, 27.68, 29.27, <b>31.78</b> , 32.85, 38.83, 43.10, 44.30, 47.78, 47.94, 52.71, 56.25, 57.20, 58.68, 59.34, 63.53, 67.30, 69.34, 69.99, 73.99, 77.77, 79.07	00-006-0464
Cu <sub>2</sub> S	15.91, 22.58, 27.76, 32.11, 36.10, 39.64, <b>46.10</b> , 51.92, 54.67	00-053-0522
SnS	22.01, 26.00, 27.47, 30.47, <b>31.53</b> , 31.97, 39.04, 45.49, 48.50, 51.31, 53.14	00-039-0354
SnS <sub>2</sub>	<b>15.02</b> , 28.19, 30.26, 32.12, 41.88, 46.12, 49.96, 52.45	00-023-0677
Sn <sub>2</sub> S <sub>3</sub>	12.63, 16.10, <b>21.49</b> , 23.77, 27.33, 27.68, 30.91, 32.53, 33.53, 33.79, 35.89, 36.49, 37.93, 39.85	00-014-0619
ZnS	<b>28.42</b> , 32.93, 47.27, 56.08, 58.81, 69.08, 76.32, 78.68 (cubic); <b>26.91</b> , 28.50, 30.52, 39.61, 47.56, 51.77, 55.49, 56.39, 57.57, 59.00, 63.55, 66.00, 72.92, 76.03, 77.81, 79.05 (hexagonal)	01-071-5976 (cubic); 00-036-1450 (hexagonal)
MoS <sub>2</sub>	<b>14.37</b> , 29.02, 32.67, 33.50, 35.87, 39.53, 44.15, 49.78, 55.97, 58.33, 60.14, 62.81, 66.46, 68.47, 68.99, 70.14, 72.78, 75.98, 77.57, 78.11, 80.18, 85.16, 86.71	00-037-1492

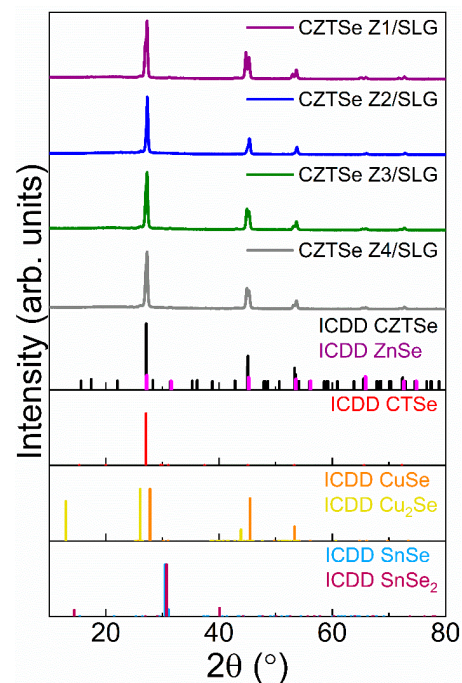


**Figure 8.** X-ray diffractograms of CZTSe films deposited on SLG using different stacks. Reproduced with permission [69].

**Table 2.** CZTSe and most frequent secondary phases main XRD peaks following their ICDD cards. The most intense peak of each phase is bolded.

Compound	Most Intense XRD Peaks (°)	ICDD Card Number
Cu <sub>2</sub> ZnSnSe <sub>4</sub>	15.61, 17.41, 22.06, <b>27.14</b> , 28.31, 35.25, 36.12, 38.81, 42.78, 42.88, 45.00, 45.09, 48.60, 53.34, 53.51, 54.10, 60.90, 63.83, 65.53, 65.81, 68.59, 72.29, 72.43, 72.87, 72.93, 83.10, 83.29	04-019-1866
Cu <sub>2</sub> SnSe <sub>3</sub>	<b>27.09</b> , 31.38, 44.97, 53.29, 55.86, 65.49, 72.23, 74.42 (cubic); 15.33, 19.99, <b>27.08</b> , 29.66, 29.98, 31.02, 37.45, 45.06, 53.28, 65.60, 72.30 (monoclinic)	03-065-7524 (cubic); 00-056-1111 (monoclinic)
CuSe	25.70, 26.29, <b>27.80</b> , 30.15, 31.01, 40.73, 45.11, 45.47, 49.75, 53.34, 54.16, 56.10, 64.82, 66.06, 69.75, 73.39	00-027-0185
Cu <sub>2</sub> Se	27.10, 31.39, <b>44.99</b> , 53.31, 55.89, 65.52, 72.26, 74.45, 83.01, 89.32 (cubic); 12.95, 25.25, 25.36, 26.07, 26.32, <b>26.44</b> , 35.88, 37.04, 38.32, 38.49, 38.68, 38.82, 39.05, 39.20, 39.31, 39.42, 39.66, 40.04, 40.27, 40.42, 40.93, 41.24, 41.34, 41.64, 41.84, 42.37, 43.00, 43.20, 43.57, 43.88, 44.16, 44.34, 44.42, 44.95, 47.92, 48.88, 49.89, 51.23, 51.51, 51.71, 51.85, 52.01, 52.32, 52.64; (monoclinic)	01-088-2043 (cubic) 00-058-0228 (monoclinic)
SnSe	15.40, 21.47, 25.31, 26.45, 29.42, <b>30.46</b> , 31.08, 37.28, 37.78, 38.03, 40.58, 41.36, 43.34, 43.53, 44.32, 47.04, 47.25, 49.10, 49.71, 51.04, 51.95, 52.04, 52.43, 52.55, 54.47, 56.85, 57.66, 60.00, 61.05, 61.63, 62.22, 63.31, 63.90, 66.21, 67.07, 67.79, 69.10	00-048-1224
SnSe <sub>2</sub>	14.42, 26.99, 29.07, <b>30.73</b> , 40.09, 44.23, 47.68, 50.08, 52.59, 55.65, 56.82, 57.81, 60.27, 64.01, 67.07, 67.23, 73.70, 76.26, 77.74, 78.11, 80.267	01-089-2939
ZnSe	<b>27.13</b> , 31.43, 45.05, 53.38, 55.96, 65.61, 72.37, 74.56, 83.14	01-071-5978
MoSe <sub>2</sub>	13.68, 27.57, 31.38, 32.15, 34.37, <b>37.83</b> , 41.89, 42.25, 47.45, 53.26, 55.86, 56.93, 57.80, 59.61, 63.41, 65.48, 65.93, 66.46, 67.26, 69.45, 72.20, 72.46, 73.14, 73.82, 76.26, 80.83, 81.74, 83.87, 86.15, 90.31, 91.36, 91.36, 92.26, 92.99, 95.03, 97.90, 98.56, 99.22, 99.72	04-004-8782

### Raman Spectroscopy

The detection of secondary phases in CZT(S/Se) films presents distinct challenges when employing only XRD. This technique relies on the distinct patterns of diffraction peaks to identify different phases based on their crystal structures. As shown, CZT(S/Se) and certain secondary phases may exhibit similar XRD patterns due to comparable crystal structures, making their differentiation challenging. On the other hand, Raman spectroscopy offers a complementary approach. It is highly sensitive to molecular vibrations and provides detailed information about chemical composition. Raman spectra can reveal unique vibrational modes for each phase, offering a more specific fingerprint for identification. Despite the challenge of similar XRD patterns in CZT(S/Se), Raman spectroscopy becomes a valuable tool in distinguishing secondary phases, providing a nuanced analysis of the molecular composition and facilitating a more precise characterization of complex CZT(S/Se) thin films. However, few signals of some secondary phases can also overlap with the main CZTS or CZTSe phases, making it challenging to precisely identify secondary phases. Additionally, the laser power used in Raman spectroscopy may induce

sample heating, potentially altering the material properties during analysis. Another notable disadvantage of micro-Raman spectroscopy in the context of CZT(S/Se) films is its inherently localized analysis. The technique typically probes a small area of the sample, which can be a limitation when dealing with heterogeneous films or when aiming for a comprehensive understanding of the material across larger surfaces. This localized nature may lead to a potential oversight of variations in secondary phase distribution throughout the sample, for that reason, it is mandatory to perform several analyses on different areas of the sample. In addition, one of the Raman spectroscopy aspects is its sensitivity to the excitation wavelength. Different phases within CZT(S/Se) films may exhibit distinct Raman signatures under specific excitation wavelengths. This wavelength dependence can be advantageous for selectively probing certain phases, enhancing the specificity of the analysis. However, it also introduces a challenge because optimal wavelengths for one phase might not be suitable for others. Therefore, the choice of excitation wavelength in Raman spectroscopy is an important consideration, and a comprehensive understanding of the material may require experimentation with various wavelengths to ensure effective detection and characterization of all relevant phases. Therefore, careful consideration of these advantages and limitations is crucial when employing Raman spectroscopy for secondary phase detection, necessitating complementary techniques to ensure comprehensive and accurate characterization of these thin films.

Various wavelengths from UV to IR can be used to identify the CZTS phase in thin films. Green or red excitation wavelengths (514, 532 and 633 nm) are commonly used to observe the vibrational modes of the CZTS phase, and the main peaks are located at 287, 337, 266 and 374  $\text{cm}^{-1}$ . Demitrievska et al. [70], realized a complete analysis of all Raman active modes by measuring CZTS films under six different excitations. Through their work they discovered additional CZTS peaks accumulating a total of 18 peaks attributed to 27 optical modes relative to the kesterite phase, as summarized Table 3. Regarding secondary phases and in contrast to XRD, Raman spectroscopy proves advantageous in the straightforward identification of secondary phases like ZnS and various structures of CTS in CZTS films. While CZTS is commonly analyzed using green or red excitation wavelengths, the detection of ZnS requires UV light (325 nm exclusively), due to its resonance characteristics (typically 347–350  $\text{cm}^{-1}$ ), and to the fact that ZnS has a bandgap close to the 325 nm wavelength (3.8 eV) [71]. Furthermore, CTS crystallizes in three distinct structures (cubic, monoclinic, and tetragonal) each characterized by unique Raman peaks. In a previous work, we studied the polymorphic nature of CTS films prepared by magnetron sputtering of two different stacks (SLG/SnS<sub>2</sub>/Cu and SLG/Cu/SnS<sub>2</sub>) annealed at different temperatures and in different atmospheres. We have tried to compare Raman spectra of the CTS films with the reported values in the literature (Figure 9a). It was found that the literature regarding the assignment of Raman modes to the three Cu<sub>2</sub>SnS<sub>3</sub> structures create challenges. While agreement exists on the main Raman peaks for each structure, such as 290  $\text{cm}^{-1}$  for monoclinic CTS, 303  $\text{cm}^{-1}$  for cubic CTS, and 337  $\text{cm}^{-1}$  for tetragonal CTS, contradictions arise in assigning other modes. The modes at 350–354  $\text{cm}^{-1}$ , the peaks between 292–295  $\text{cm}^{-1}$  and at 370–374  $\text{cm}^{-1}$  are debated between different phases of the Cu-Sn-S family. This complexity extends to the Raman modes in the region 314–318  $\text{cm}^{-1}$ , which could belong to Cu<sub>x</sub>Sn<sub>y</sub>S<sub>z</sub> or SnS<sub>2</sub> according to different studies [72–75]. If the analyzed samples contain zinc, some of the previously listed peaks can overlap with other phases. For instance, the peaks at 315 and 353  $\text{cm}^{-1}$ , which are indicative of CZTS, may also represent other phases (for instance SnS at 314  $\text{cm}^{-1}$  and CTS at 353  $\text{cm}^{-1}$ , respectively). Additionally, the peak at 350  $\text{cm}^{-1}$ , typically associated with the ZnS phase, further increase the complexity of the identification process. Similarly, for the CuS secondary phase, the primary mode is at 465–467  $\text{cm}^{-1}$ , accompanied by another smaller peak at 261–264  $\text{cm}^{-1}$  (Figure 9b), which may lead to potential uncertainty with the 262  $\text{cm}^{-1}$  CZTS mode. In the case of SnS, the main peak appears at 190–192  $\text{cm}^{-1}$ , accompanied by a less intense peak at 160–164  $\text{cm}^{-1}$ , posing a possible misinterpretation as CZTS has a peak at 164  $\text{cm}^{-1}$ . The

other frequently occurring secondary phases in the CZTS system, such as  $\text{Cu}_2\text{S}$ ,  $\text{Sn}_2\text{S}_3$ , and  $\text{MoS}_2$ , exhibit distinct Raman modes, making them easily detectable (Table 3).

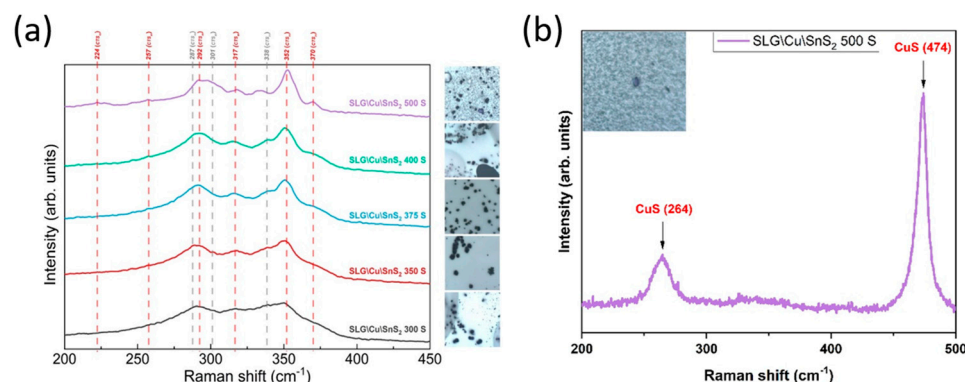


**Figure 9.** Raman spectra of (a) SLG/SnS<sub>2</sub>/Cu stacks annealed in S atmosphere at different temperatures and (b) Raman spectra of CuS secondary phase depicted in one of the SLG/SnS<sub>2</sub>/Cu films annealed at 500 °C. Figures were reproduced with permission [20].

**Table 3.** Raman peaks of CZTS and most common secondary phases. The highest peak of each phase is bolded.

Compound	Raman Shift (cm <sup>-1</sup> )	References
$\text{Cu}_2\text{ZnSnS}_4$	67, 81, 96, 139, 150, 164, 255, 262, 271, 287, 302, 315, <b>331</b> , <b>337</b> , 347, 353, 366, 374	[70]
$\text{Cu}_2\text{SnS}_3$	267, 299, 302, <b>302–303</b> , 351, 354–356, 365 (cubic); 222–225, 249–250, 254–255, 258, 268, 287, <b>290–295</b> , 314–317, 346–348, 349–354, 371–374 (monoclinic); 286, 289, 297, 300, 317, 330–331, <b>334–337</b> , 343, 351–353, 356 (tetragonal)	[76]
CuS	261–264, <b>465–467</b>	[77]
$\text{Cu}_2\text{S}$	<b>472–475</b>	[78]
SnS	93–95, 160–164, <b>190–192</b> , 218	[79,80]
$\text{SnS}_2$	<b>312–314</b>	[81,82]
$\text{Sn}_2\text{S}_3$	232, <b>305–308</b>	[81,82]
ZnS	<b>350</b> , 697, 1045	[83,84]
$\text{MoS}_2$	385, <b>403–405</b>	[85,86]

In contrast to XRD, where it is advised to depend on minor peaks for distinguishing between secondary phases and the primary CZTS phase, in Raman spectroscopy, the most intense modes of all phases are distinct, while the minor peaks can occasionally lead to uncertainty.

In the same manner, Raman spectroscopy serves as a valuable tool for discerning secondary phases in CZTSe compounds. This technique aids in the identification of various phases through the analysis of their distinct Raman modes. However, the interpretation of Raman spectra in CZTSe is not without challenges, and there may be discrepancies in assigning specific modes to certain structural features. The most common Raman modes relative to the CZTSe phase are 173, 195, 232, and 244 cm<sup>-1</sup> as shown by Zaki et al. in a study of  $\text{Cu}_2\text{ZnSnSe}_4$  films synthesized from different stacks and shown in Figure 10 [87]. However, an investigation by Dimitrievska et al. [88] has facilitated the discovery and identification of novel Raman modes associated with the CZTSe phase. In their study they prepared CZTSe absorbers by annealing a Sn/Cu/Zn stack in a graphite box containing Sn and Se powders. The resulted films were then extensively analyzed by Raman spectroscopy

using nine different excitation wavelengths (325, 442, 457.9, 514.5, 532.1, 632.8, 784.6, 830 and 1064 nm). They stated that the exploration of Raman spectroscopy in CZTSe reveals a capability to influence the intensities of intrinsic Raman peaks when using different wavelengths. While this enhancement can reveal previously unreported Raman peaks (55, 80, 135, 158, 171, 188, 213, 251  $\text{cm}^{-1}$ ), caution is warranted as it might introduce misinterpretations. Here as well, while the detection of secondary phases is facilitated by their distinctive and intense Raman peaks, a challenge arises with the less intense peaks, as they may overlap with CZTSe peaks. In fact, the Raman modes of cubic CTSe (236  $\text{cm}^{-1}$ ), monoclinic CTSe (230  $\text{cm}^{-1}$ ), and CZTSe (232–234  $\text{cm}^{-1}$ ) present a challenge due to the closely similar relative peaks position. However, the CTSe phase in both structures can be easily detected when relying on the other peaks presented in Table 4. Furthermore, the overlapping of tiny peaks at 242  $\text{cm}^{-1}$  between  $\text{MoSe}_2$  and CZTSe introduces complexity to the identification process. It is noteworthy that the most intense peak of ZnSe at 250  $\text{cm}^{-1}$  as well poses potential confusion with the small peaks of cubic CTSe at 252  $\text{cm}^{-1}$ , monoclinic CTSe at 248  $\text{cm}^{-1}$  and CZTSe at 251  $\text{cm}^{-1}$ . A meticulous examination is imperative to navigate through these complexities and ensure accurate interpretation. The distinctiveness of the Raman peaks of other secondary phases such as  $\text{Cu}_{2-x}\text{Se}$ , SnSe, and  $\text{SnSe}_2$  stands as an advantage, facilitating their clear discrimination from those of CZTSe. In addition to the nuanced analysis of Raman spectra, complementary analyses such as scanning electron microscopy coupled with energy-dispersive X-ray spectroscopy provides valuable insights into the morphology and composition of the materials under investigation, offering a comprehensive understanding of their structural and elemental properties.

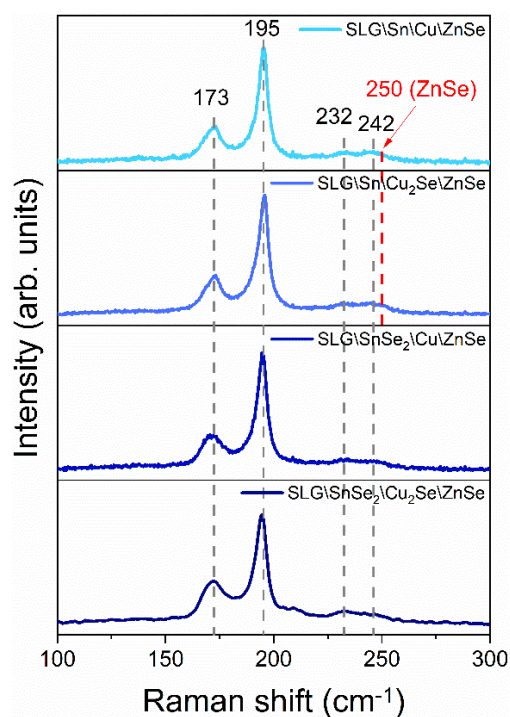


**Figure 10.** Raman spectra of CZTSe films from different stacks. The figure is reproduced with permission [87].

**Table 4.** Raman peaks of CZTSe and most common secondary phases. The highest peak of each phase is bolded.

Compound	Raman Shift (cm <sup>-1</sup> )	References
Cu <sub>2</sub> ZnSnSe <sub>4</sub>	55, 80, 135, 158, 171, 173–176, 181, <b>195–196</b> , 213, 220, 232–234, 242–244, 251	[88]
Cu <sub>2</sub> SnSe <sub>3</sub>	68, 77, <b>180</b> , 200, 236, 252 (cubic); 66, 76, <b>179</b> , 203, 210, 230, 248 (monoclinic)	[89,90]
Cu <sub>2-x</sub> Se	<b>258–262</b>	[91]
SnSe	33, 71, <b>108</b> , 130, 150	[92]
SnSe <sub>2</sub>	119, <b>185</b> , 314	[58]
ZnSe	206, <b>250</b>	[93]
MoSe <sub>2</sub>	<b>242</b> , 285	[94]

### 3.2.2. Morphological and Compositional Analysis

#### SEM-EDX

While scanning electron microscopy (SEM) and energy-dispersive X-ray spectroscopy (EDS) are valuable techniques for examining the morphology and elemental composition of materials, they may not be as effective in directly identifying secondary phases in CZTS and CZTSe films compared to previously described techniques. SEM provides high-resolution images of the surface, revealing details about the film structure, grain boundaries, and other morphological features. EDS, on the other hand, detects the elemental composition. However, identifying secondary phases often requires information about the crystal structure, which is more effectively obtained through techniques like XRD or Raman spectroscopy.

In spite of that, SEM and EDS and/or EDS mapping analyses can still provide valuable indirect indicators of the presence of secondary phases in CZTS and CZTSe films. Differences in grain shapes and sizes observed through SEM images may suggest a heterogeneous composition, hinting at the possible existence of multiple phases [95]. Moreover, off-stoichiometric compositions, where certain elements are in excess, may raise suspicions about the formation of secondary phases [96]. An elevated concentration of certain elements not corresponding to the desired kesterite composition can signify the presence of secondary phases. EDS mapping is particularly useful in this context, as it can reveal spatial variations in elemental distribution. Regions with higher concentrations of specific elements may correspond to secondary phases, and this can be visually represented by denser and colored areas in the EDS maps [97].

For instance, the detection of Cu<sub>2</sub>S secondary phase in CZTS films can be achieved through SEM analysis. By examining the surface morphology of the films, isolated large grains can be observed, often distributed non-uniformly across the surface. These large grains, indicative of Cu<sub>2</sub>S crystallites [98,99]. Additionally, the use of EDS further confirms the presence of Cu<sub>2</sub>S by analyzing the elemental composition of these large grains. The combination of SEM and EDS provides an effective method for identifying and characterizing Cu<sub>2</sub>S secondary phase in CZTS films, aiding in the comprehensive analysis of their structural composition as reported in various studies [100,101]. Similarly, Buffiere et al., discovered particles measuring around 80 nm, situated at the base of the CZTSe film, which when analyzed by EDS found to be rich in Cu and Se, meaning the presence of Cu<sub>2</sub>Se [102]. The same observations were reported by Fella et al., in another study [103]. Contrarily, Zn(S/Se) particles are mainly located at the bottom and may appear as small, distinct entities, often distinguished by their morphology or contrast within the micrograph [104]. Bishop et al., revealed that the presence of ZnSe can be distinctly highlighted through illuminated charging regions in SEM images of their CZTSe films, particularly when employing in-lens secondary electron detection [105]. The in-lens detector boasts enhanced efficiency in capturing low-energy electrons, resulting in a superior signal-to-noise ratio. This improved efficiency and signal quality contribute to heightened contrast, facilitating clearer visibility

and differentiation of impurities. Similar conclusions were drawn in these studies on CZTS films, where bright particles were observed and when analyzed by EDS showed compositions rich in zinc and sulfur, aiding in the identification and confirmation of the ZnS secondary phase in the CZTS films [106,107]. On the other hand, the identification of SnS and SnS<sub>2</sub> secondary phases in CZTS films is facilitated through various SEM and EDS observations. Zaki et al., detected the presence of larger white particles, exceeding the size of CZTS grains, corresponds to the SnS<sub>2</sub> secondary phase, as confirmed by EDS mapping and shown in Figure 11 [65]. In other studies, SEM images reveal sheet-like structures identified as SnS<sub>2</sub> on the surface of CZTS films, EDX mapping further substantiates the presence of Sn and S elements in the identified sheet-like grains [108,109]. Additionally, the SnS phase is discernible as flake-like features in CZTS films, evident in SEM images and verified by EDX analysis in an investigation by Engberg et al. [110]. Similarly, the detection of SnSe<sub>x</sub> secondary phases in CZTSe films involves SEM imaging and EDS analysis. Lin et al., observed distinct morphologies when analyzing CZTSe films, categorized as a rod-like appearance and a round or semicircular shaped grains. By measuring EDS analysis on these morphologies, they confirmed their predominantly comprising Sn and Se elements, which is synonym of SnSe<sub>2</sub> presence [111]. Temgoua et al., stated that the SnSe<sub>2</sub> compounds can be spotted as hexagonal structures on the surface of CZTSe [112]. Furthermore, the SEM images of CZTSe absorbers realized by Becerril-Romero et al., revealed elongated grains (SnSe<sub>x</sub>), which consist of mainly Sn and Se elements after EDX measurements [113]. Additionally, cross-sectional SEM images can reveal the layered structure of thin films. In the case of CZTS and CZTSe films, the presence of secondary phases like molybdenum disulfide and molybdenum diselenide can be discerned through these images [114]. Specifically, Mo(S/Se)<sub>2</sub> tends to form a thin layer situated between the Mo substrate and the CZTS or CZTSe layer. The distinct visual separation in the cross-sectional view helps in identifying and confirming the presence of this secondary phases [115,116]. These observations from cross-sectional SEM provide valuable insights into the structural composition of the films, aiding in a comprehensive understanding of their layered architecture and the potential existence of additional phases.

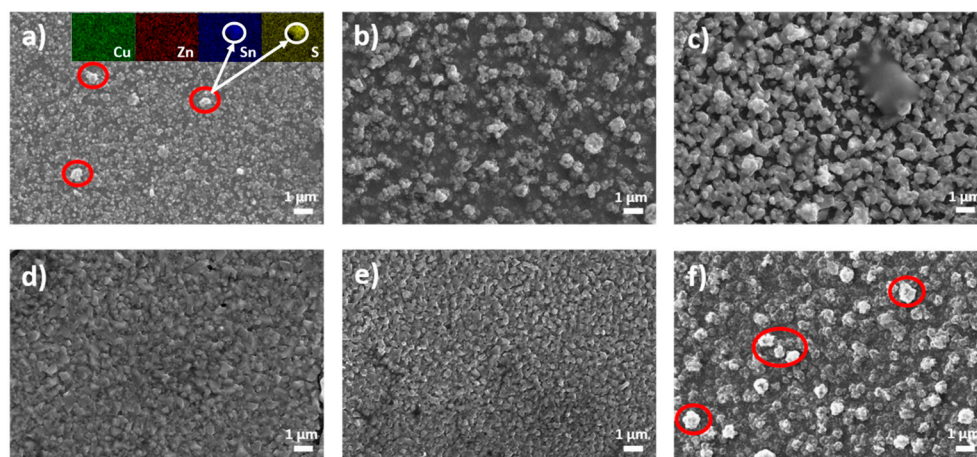


**Figure 11.** SEM images of the CZTS films from SLG\CTS\ZnS-150 stack annealed in Sn + S atmosphere for (a) 30, (b) 45, and (c) 60 min, respectively; and the SLG\CTS\ZnS-200 stack sulfurized for (d) 30, (e) 45, and (f) 60 min, respectively. The red circles represent grains of the SnS<sub>2</sub> secondary phase; the inset shows the SnS<sub>2</sub> grains observed by EDS mapping. Reproduced with permission [65].

There is consensus among researchers regarding the distinctive features of certain secondary phases in CZTS and CZTSe films. Large grains correspond to Cu<sub>2</sub>S and Cu<sub>2</sub>Se, while smaller white spots, notably visible in contrast, are indicative of ZnS or ZnSe. Similarly, SnS<sub>2</sub> is identified as large grains at the surface of the film, and SnSe<sub>2</sub> manifests as round-shaped discs or hexagonal structures easily distinguishable as represented in Figure 12. A thin layer of MoS<sub>2</sub> or MoSe<sub>2</sub> is typically observed between the molybdenum

substrate and the CZTS or CZTSe layer, respectively. However, some secondary phases elude detection through SEM or EDX, and their identification through these techniques remains unreported. While the combination of SEM imaging and EDX mapping is valuable for detecting and characterizing various secondary phases, it is essential to acknowledge the limitations, as some of the secondary phases (such as CTS or CTSe) cannot be observed through SEM or identified by EDX and their definitive identification may require complementary methods such as XRD or Raman spectroscopy.

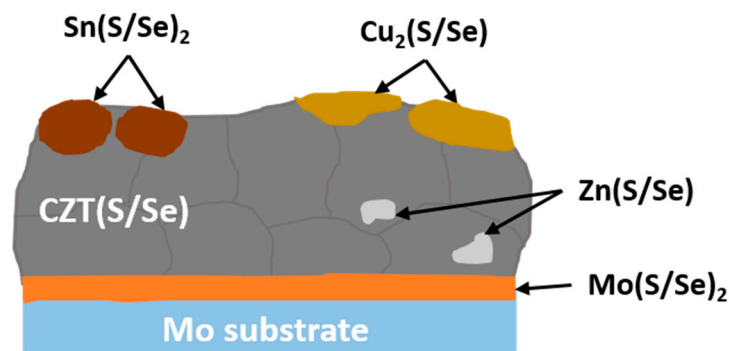


**Figure 12.** Representation of the distribution and morphology of  $\text{Cu}_2(\text{S/Se})$ ,  $\text{Sn}(\text{S/Se})_2$ ,  $\text{Zn}(\text{S/Se})$  and  $\text{Mo}(\text{S/Se})_2$  secondary phases within the  $\text{CZT}(\text{S/Se})$  film.

### 3.3. Strategies to Enhance Phase Control

Achieving single-phase CZTS and CZTSe absorber layers has posed challenges due to the tendency for secondary phase formation. The abundance of studies reporting the coexistence of these secondary phases has highlighted the complexities involved. However, amidst these challenges, obtaining single-phase CZTS and CZTSe is achievable. Two main strategies are employed to address and remove secondary phases, ensuring the attainment of single-phase CZTS or CZTSe films. The first approach involves prevention through the meticulous optimization of deposition parameters by fine-tuning the synthesis conditions to avoid the formation of undesired secondary phases. The second strategy employs etching techniques. When secondary phases are present on the surface, etching methods can effectively remove them, leaving behind a purified CZTS or CZTSe structures.

Optimizing the growth conditions, such as deposition temperature, time, and rates, influences crystal structure and minimizes secondary phase occurrence [117,118]. Stoichiometry control during fabrication is also important, by ensuring accurate control over the precursor ratios and compositions during deposition. Post-deposition annealing under controlled atmospheres aids in achieving better phase purity by facilitating atomic rearrangements. Improvements in sulfurization or selenization parameters such as temperature, time, and atmosphere are essential to enhance the incorporation of sulfur or selenium and reduce secondary phases. Besides optimizing the deposition parameters, researchers have explored inventive approaches to improve this process. Comparison of annealing atmospheres, temperatures, and annealing time across different studies reveals variations in phase purity achieved, highlighting the importance of optimizing annealing conditions for controlling secondary phase formation in  $\text{CZT}(\text{S/Se})$  thin films [119–121]. For instance, the addition of Sn with sulfur or selenium during annealing has been found effective in reducing Sn losses, contributing to improved stoichiometry and minimizing secondary phases [122,123]. Additionally, the use of a graphite box during annealing offers distinct advantages. The graphite box acts as a protective shield, preventing the loss of volatile elements and maintaining the required sulfur or selenium content. This controlled atmosphere during annealing facilitates better compositional stability and reduces the likelihood of secondary phase formation [124,125].

In certain studies, researchers have employed a two-step deposition strategy, involving the sequential deposition of  $\text{Cu}_2\text{SnS}_3$  or  $\text{Cu}_2\text{SnSe}_3$  followed by a layer of ZnS or ZnSe as

presented in Figure 11a–c). Various techniques, including hydrothermal [126], spray pyrolysis [127], chemical bath deposition [128], sonochemical reactions [129], and magnetron sputtering [65,87], have effectively employed a two-step synthesis process. This innovative approach is effective in mitigating secondary phases when the process is meticulously optimized. The rationale behind this two-step deposition is to carefully control the precursor materials, and deposition parameters at each stage. Figure 13 is a schematic of the two-step synthesis process, for both CZTS and CZTSe phases. In the first stage, the focus is on achieving a single-phase CTS or CTSe film devoid of secondary phases. This initial step requires meticulous control of precursor materials, concentrations, and deposition parameters to ensure the desired phase purity. Once an optimized CTS or CTSe film is obtained, the second stage involves the addition of a carefully optimized layer of ZnS or ZnSe. This subsequent layer reacts with the existing CTS or CTSe film during the annealing processes, fostering the formation of the desired CZTS or CZTSe phase. The controlled interaction between the layers is a key aspect of this approach, aiming to enhance the crystallinity and phase purity of the final CZTS or CZTSe film while mitigating the presence of undesirable secondary phases. This nuanced two-step deposition process illustrates a strategic methodology to achieve high-quality, single-phase CZTS and CZTSe absorber layers for improved solar cell performance.

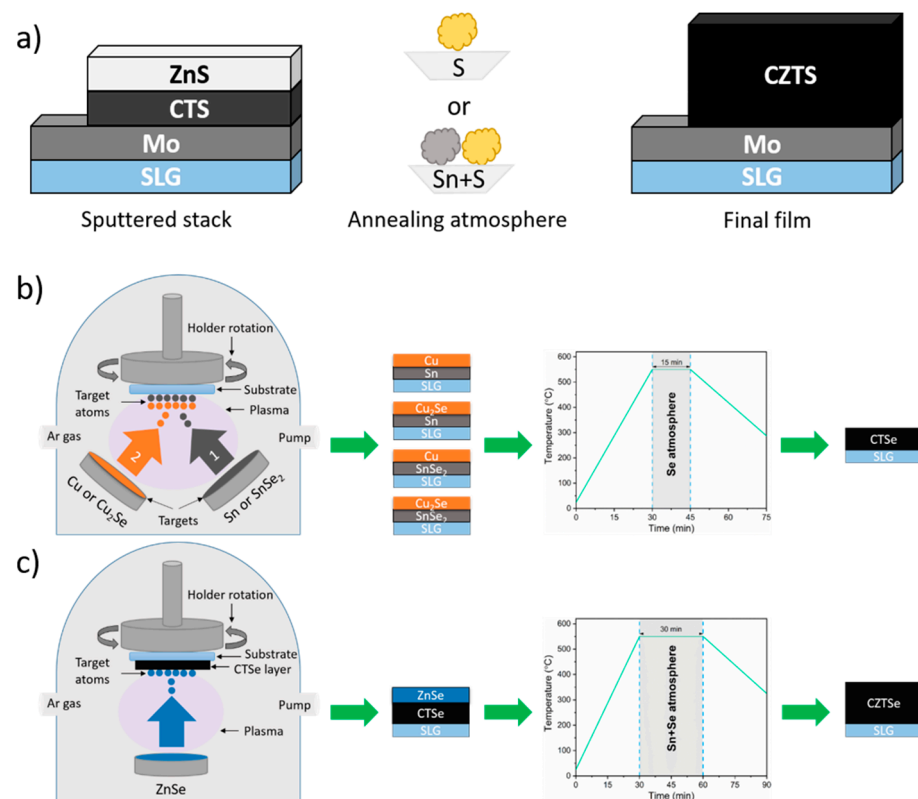


**Figure 13.** Schematic of the magnetron sputtering deposition and annealing process of (a) the CZTS films (b) the CTSe layer and (c) the CZTSe final films. Reproduced with permission [65,87].

On the other hand, chemical etching emerged as a tool for eliminating secondary phases CZTS and CZTSe films. Various etching methods have been employed to selectively remove specific secondary phases, contributing to the production of single-phase absorber layers. For Cu(S/Se) secondary phases, a common solution is the use of KCN etching, a method established through routine application in the processing of CIGSSe films and effectively adaptable to kesterites as well [66,130]. ZnS, when present, can be successfully eliminated by immersing the film in a 5–10% hot HCl solution at 75 °C [131]. The removal of ZnSe often involves an oxidation route, where  $\text{KMnO}_4/\text{H}_2\text{SO}_4$  is applied followed by

a Na<sub>2</sub>S solution rinse, proving to be an effective technique [132]. To address Sn(S,Se)<sub>2</sub> secondary phases, (NH<sub>4</sub>)<sub>2</sub>S etching solution has been identified as a promising approach, offering a potential possibility to mitigate the presence of these unwanted phases [133,134]. In a separate investigation conducted by Wang et al. [109], they demonstrated the successful removal of the SnS<sub>2</sub> secondary phase located on the surface of the CZTS thin film. This was achieved through a method involving physical adhesion, utilizing a conductive tape known for its resistance to debonding. These selective etching routes provide targeted solutions for specific secondary phases, contributing to the enhancement of CZTS and CZTSe film purity.

#### 4. Influence of Secondary Phases on the Solar Device Efficiency

Although the exact impact of residual secondary phases on the performance of kesterite-based solar cells remains poorly understood, recent research suggests that the presence of secondary phases in CZT(S/Se) thin-film solar cells can significantly impact their efficiency and stability [135,136]. These secondary phases, such as CTS, Cu<sub>x</sub>S, ZnS, Sn<sub>x</sub>S<sub>y</sub>, in the CZTS compound and similarly, CTSe, Cu<sub>x</sub>Se, ZnSe, and Sn<sub>x</sub>Se<sub>y</sub>, for CZTSe, often act as recombination centers for charge carriers, leading to increased non-radiative recombination losses. This hinders the overall charge transport within the material, ultimately reducing the solar cell performance. Moreover, the formation of secondary phases can introduce defects and grain boundaries, causing additional electron-hole recombination sites and reducing carrier lifetime. As a consequence, the device power conversion efficiency is adversely affected. The presence of various secondary phases in CZTS-based solar cells significantly impacts their performance. For instance, ZnS, characterized by a wide band gap of 3.5 eV, acts as an insulator, reducing the effect sunlight-absorbing area available for generating electron-hole pairs leading to a decrease in current collection [137]. On the other hand, highly conductive Cu<sub>2</sub>S may create short circuits in solar cells, potentially compromising their efficiency [138]. However, another investigation revealed that the presence of the Cu<sub>2</sub>S secondary phase is not detrimental to the photovoltaic performance of CZTS [139]. On the contrary, it was found that the Cu<sub>2</sub>S phase might play a constructive role, potentially contributing to the enhancement of the overall photovoltaic performance. SnS<sub>2</sub>, being an n-type semiconductor with a band gap of approximately 2.2 eV, has the potential to form a pn junction with the absorber layer, acting as a barrier to charge collection and leading to increased photocarrier recombination [74]. The presence of Cu<sub>2</sub>SnS<sub>3</sub> (CTS), observed in Zn-poor CZTS cells, is noteworthy. While CTS is a p-type semiconductor with a band gap similar to CZTS, recent studies suggest its lower efficiency compared to CZTS thin films, highlighting the potential detrimental impact of this unwanted secondary phase on CZTS solar cell performance [140].

In the context of CZTSe solar cells, the presence of secondary phases, notably ZnSe and MoSe<sub>2</sub>, poses challenges related to increased series resistance, potentially impeding the efficient flow of current [141,142]. SnSe<sub>2</sub> adversely impacted solar cell performance by diminishing shunt resistance [112]. Furthermore, the high conductivity inherent in Cu–Se phases can potentially lead to shunting in CZTSe solar cells, further influencing their photovoltaic performance [143]. Additionally, the emergence of Cu<sub>2</sub>SnSe<sub>3</sub> phases in CZTSe absorber layers may contribute to a decrease in the open-circuit voltage (Voc) [144]. This effect is important, especially considering the energy bandgap variations ( $E_g = 0.84$  eV). For that reason, it is mandatory to understand and mitigate these specific influences of secondary phases for optimizing CZTSe-based solar devices.

Figure 14 compares the highest efficiencies achieved in solar cells based on CZTS and CZTSe absorber layers deposited by various methods, considering the presence or absence of secondary phases. Among the electrodeposition techniques, CZTS devices reached a peak efficiency of 7.30% in the absence of secondary phases [145], while CZTSe solar cells achieved 8.20% [146]. However, when secondary phases were present, the efficiency slightly decreased to 7.10% for CZTS [118] and 7% for CZTSe [114]. Sol-gel deposition yielded 8.84% efficiency for solar devices based on single-phase CZTS films [147],

but only 5.10% when secondary phases were present [148]. In spray pyrolysis, CZTS achieved 6.40% efficiency without secondary phases [149], whereas the CZTSe-based device reached 6.80% [150]. Evaporation techniques resulted in the good efficiencies, with CZTS absorbers reaching 9.20% without secondary phases [151] and CZTSe absorbers achieving 11.70% [152]. However, the presence of secondary phases slightly reduced the efficiency to 8.90% for CZTSe [153]. The CZTS absorber layer deposited by PLD resulted in a device achieving an efficiency of 6.62% [154]. The highest efficiencies were recorded on the devices obtained by magnetron sputtering, particularly for CZTSe films, with efficiencies of 12.50% for single-phase films [155] and 11.40% for films with secondary phases [156]. While for the CZTS material, the efficiency is a bit lower with 11.01% for the single phase-based device [157] and 9.70% in the presence of secondary phases [158].

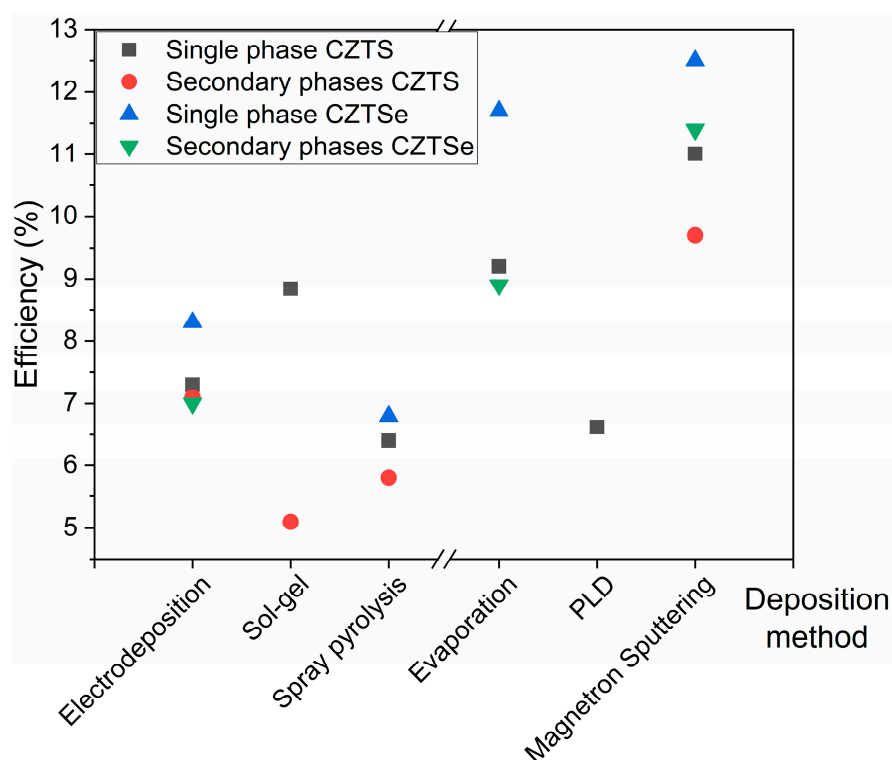


**Figure 14.** Efficiency comparison of CZTS and CZTSe films deposited by various methods, with and without the presence of secondary phases.

Table 5 summarizes the performance of CZTS and CZTSe devices fabricated by using some of the described deposition techniques. Solar devices with a single-phase CZTS or CZTSe exhibit higher efficiencies compared to those with the presence of secondary phases. Furthermore, we found that CZTSe consistently outperforms CZTS in terms of efficiency, regardless of the deposition technique employed. This superior performance of CZTSe can be attributed to its optimal bandgap alignment, offering improved light absorption and electron-hole pair generation, ultimately enhancing the overall efficiency of the solar device. However, the highest recorded efficiency in solar devices was achieved with a CZTSSe-based solar cell (13.6%) [159], when combining the advantages of both CZTS and CZTSe materials. By understanding and effectively controlling the formation of these unwanted phases, through careful optimization of deposition methods, post-deposition annealing treatments, and compositional engineering, researchers can pave the way for the development of high-performance CZT(S/Se) thin-film solar cells, contributing to the advancement of renewable energy technologies.

**Table 5.** Comparison of efficiencies in different CZTS and CZTSe single phases cells and the influence of the of secondary phases, depending on the depositions method.

Deposition Method	PCE (%)			
	Single Phase CZTS	Secondary Phases CZTS	Single Phase CZTSe	Secondary Phases CZTSe
Electrodeposition	7.30 [145]	7.10 [118]	8.20 [146]	7 [114]
Sol-gel	8.84 [147]	5.10 [148]	-	-
Spray pyrolysis	6.40 [149]	5.80 [160]	6.80 [150]	-
Evaporation	9.20 [151]	-	11.70 [152]	8.90 [153]
PLD	6.62 [154]	-	-	-
Magnetron sputtering	11.01 [157]	9.70 [158]	12.50 [155]	11.40 [156]

## 5. Conclusions

In summary, this review has explored the field of kesterite materials, with a particular focus on the formation and controlling of secondary properties in CZTS and CZTSe films. By describing a range of deposition techniques, spanning from solution-based methods like electrodeposition, sol-gel and spray pyrolysis to vacuum methods such as evaporation, pulsed laser deposition, and magnetron sputtering, we have highlighted the diverse approaches employed in single phase CZTS and CZTSe synthesis. Moreover, the details associated with secondary phases formation, such as  $\text{Cu}_x(\text{S}/\text{Se})$ ,  $\text{Sn}_x(\text{S}/\text{Se})_y$ ,  $\text{Zn}(\text{S}/\text{Se})$ ,  $\text{CT}(\text{S}/\text{Se})$ , and  $\text{Mo}(\text{S}/\text{Se})_x$ , has been examined in detail, demonstrating the complexity of these materials. We have emphasized the significant role of characterization techniques like X-ray diffraction, Raman spectroscopy, and scanning electron microscopy with energy-dispersive X-ray spectroscopy in accurately identifying these phases. Furthermore, strategies aimed at mitigating or removing secondary phases have been explored, signaling a pathway toward achieving single-phase CZTS or CZTSe films. Lastly, insights into the implications of secondary phases on solar device performance have been provided, emphasizing the need for an in-depth understanding and precise control of material composition for optimal photovoltaic efficiency. Future research could explore the investigation of novel approaches to suppress secondary phase formation and enhance phase purity, leading to the development of more efficient and stable CZTS and CZTSe thin-film solar cells. Additionally, the integration of advanced characterization techniques, could provide deeper insights into the morphology and composition of kesterite thin films, facilitating further identification of subtle secondary phases. This comprehensive exploration could serve as a foundational resource to guide future research endeavors and advancements in the synthesis and utilization of CZT(S/Se) materials in solar energy conversion.

**Author Contributions:** Conceptualization, M.Y.Z. and A.V.; methodology, M.Y.Z. and A.V.; formal analysis, M.Y.Z.; resources, M.Y.Z. and A.V.; data curation, M.Y.Z.; writing—original draft preparation, M.Y.Z.; writing—review and editing, M.Y.Z. and A.V.; visualization, M.Y.Z.; supervision, A.V.; project administration, M.Y.Z. and A.V.; funding acquisition, M.Y.Z. and A.V. All authors have read and agreed to the published version of the manuscript.

**Funding:** The authors acknowledge the financial support provided by Executive Unit for Financing Higher Education, Research, Development and Innovation (UEFISCDI), within the framework of the project PN-III-P1-1.1-PD-2021-0240 (contract no. PD 41/2022) and by the Core Program of the National Institute of Materials Physics, granted by the Romanian Ministry of Research, Innovation and Digitization through the Project PC3-PN23080303.

**Data Availability Statement:** The data presented in this study are available in this article.

**Conflicts of Interest:** The authors declare no conflicts of interest.

## References

1. El Khouja, O.; Galca, A.C.; Nouneh, K.; Zaki, M.Y.; Ebn Touhami, M.; Taibi, M.; Matei, E.; Negrila, C.C.; Enculescu, M.; Pintilie, L. Structural, Morphological and Optical Properties of Cu–Fe–Sn–S Thin Films Prepared by Electrodeposition at Fixed Applied Potential. *Thin Solid. Films* **2021**, *721*, 138547. [[CrossRef](#)]
2. Paul, S.; Gulyas, I.; Repins, I.L.; Mou, S.; Li, J.V. Carrier Transport Properties in a Thin-Film Cu<sub>2</sub>ZnSnSe<sub>4</sub> Solar Cell. *Thin Solid. Films* **2019**, *675*, 103–108. [[CrossRef](#)]
3. Zaki, M.-Y.; Sava, F.; Buruiana, A.-T.; Simandan, I.-D.; Becherescu, N.; Galca, A.-C.; Mihai, C.; Velea, A. Synthesis and Characterization of Cu<sub>2</sub>ZnSnS<sub>4</sub> Thin Films Obtained by Combined Magnetron Sputtering and Pulsed Laser Deposition. *Nanomaterials* **2021**, *11*, 2403. [[CrossRef](#)] [[PubMed](#)]
4. Padhy, S.; Mannu, R.; Singh, U.P. Graded Band Gap Structure of Kesterite Material Using Bilayer of CZTS and CZTSe for Enhanced Performance: A Numerical Approach. *Solar Energy* **2021**, *216*, 601–609. [[CrossRef](#)]
5. Zaki, M.Y.; El Khouja, O.; Nouneh, K.; Ebn Touhami, M.; Matei, E.; Azmi, S.; Rusu, M.I.; Grigorescu, C.E.A.; Briche, S.; Boutamart, M.; et al. ZnS Stacking Order Influence on the Formation of Zn-Poor and Zn-Rich Cu<sub>2</sub>ZnSnS<sub>4</sub> Phase. *J. Mater. Sci Mater. Electron.* **2022**, *33*, 11989–12001. [[CrossRef](#)]
6. El Khouja, O.; Galca, A.C.; Zaki, M.Y.; Talbi, A.; Ahmoum, H.; Nouneh, K.; Ebn Touhami, M.; Taibi, M.; Matei, E.; Enculescu, M.; et al. Secondary Phases and Their Influence on Optical and Electrical Properties of Electrodeposited Cu<sub>2</sub>FeSnS<sub>4</sub> Films. *Appl. Phys. A* **2021**, *127*, 887. [[CrossRef](#)]
7. Zhang, Y.; Zhou, S.; Sun, K. Cu<sub>2</sub>ZnSnS<sub>4</sub> (CZTS) for Photoelectrochemical CO<sub>2</sub> Reduction: Efficiency, Selectivity, and Stability. *Nanomaterials* **2023**, *13*, 2762. [[CrossRef](#)] [[PubMed](#)]
8. Khaaissa, Y.; Talbi, A.; Nouneh, K.; El Khouja, O.; Ahmoum, H.; Fahoume, M. Effect of Growth Temperature on the Physical Properties of Spray Pyrolysis Deposited CZTS Films. *Mater. Today Proc.* **2022**, *66*, 252–258. [[CrossRef](#)]
9. Azmi, S.; Layachi, O.A.; Ouardi, M.E.; Khoumri, E.M.; Moujib, A.; Brouzi, A.E.; Nohair, M.; Pezzato, L.; Dabala, M. Growth of Cu<sub>2</sub>ZnSnS<sub>4</sub> Thin Film Absorber Layer on Transparent Conductive Oxides and Molybdenum Substrates by Electrodeposition for Photovoltaic Application. *Optik* **2022**, *250*, 168320. [[CrossRef](#)]
10. Hreid, T.; Li, J.; Zhang, Y.; Spratt, H.J.; Wang, H.; Will, G. Effects of Metal Ion Concentration on Electrodeposited CuZnSn Film and Its Application in Kesterite Cu<sub>2</sub>ZnSnS<sub>4</sub> Solar Cells. *RSC Adv.* **2015**, *5*, 65114–65122. [[CrossRef](#)]
11. Azmi, S.; Moujib, A.; Layachi, O.A.; Matei, E.; Galca, A.C.; Zaki, M.Y.; Secu, M.; Rusu, M.I.; Grigorescu, C.E.A.; Khoumri, E.M. Towards Phase Pure Kesterite Cu<sub>2</sub>ZnSnS<sub>4</sub> Absorber Layers Growth via Single Step Free Sulfurization Electrodeposition under a Fix Applied Potential on Mo Substrate. *J. Alloys Compd.* **2020**, *842*, 155821. [[CrossRef](#)]
12. Valdés, M.; Sánchez, Y.; Perelstein, G.; Oliva, F.; Izquierdo-Roca, V.; Rodriguez, A.P.; Saucedo, E. Influence of Co-Electrodeposition Parameters in the Synthesis of Kesterite Thin Films for Photovoltaic. *J. Alloys Compd.* **2020**, *839*, 155679. [[CrossRef](#)]
13. Shafi, M.A.; Khan, L.; Ullah, S.; Bouich, A.; Ullah, H.; Mari, B. Synthesis of CZTS Kesterite by pH Adjustment in Order to Improve the Performance of CZTS Thin Film for Photovoltaic Applications. *Micro Nanostruct.* **2022**, *164*, 107185. [[CrossRef](#)]
14. Pawar, B.S.; Pawar, S.M.; Shin, S.W.; Choi, D.S.; Park, C.J.; Kolekar, S.S.; Kim, J.H. Effect of Complexing Agent on the Properties of Electrochemically Deposited Cu<sub>2</sub>ZnSnS<sub>4</sub> (CZTS) Thin Films. *Appl. Surf. Sci.* **2010**, *257*, 1786–1791. [[CrossRef](#)]
15. Azmi, S.; Nohair, M.; El Marrakchi, M.; Khoumri, E.M.; Dabala, M. Effect of the Complexing Agents on the Properties of Electrodeposited CZTS Thin Films. In Proceedings of the 2018 7th International Conference on Renewable Energy Research and Applications (ICRERA), Paris, France, 14–17 October 2018; pp. 1346–1351.
16. Zaki, M.Y.; Nouneh, K.; Touhami, M.E.; Matei, E.; Badica, P.; Burdusel, M.; Negrila, C.C.; Baibarac, M.; Pintilie, L.; Galca, A.C. Influence of Boric Acid Concentration on the Properties of Electrodeposited CZTS Absorber Layers. *Phys. Scr.* **2020**, *95*, 054001. [[CrossRef](#)]
17. Ge, J.; Yan, Y. Controllable Multinary Alloy Electrodeposition for Thin-Film Solar Cell Fabrication: A Case Study of Kesterite Cu<sub>2</sub>ZnSnS<sub>4</sub>. *iScience* **2018**, *1*, 55–71. [[CrossRef](#)] [[PubMed](#)]
18. Amrit, P.; Jain, S.; Tomar, M.; Gupta, V.; Joshi, B. Synthesis and Characterization of Sol Gel Derived Nontoxic CZTS Thin Films without Sulfurization. *Int. J. Appl. Ceram. Technol.* **2020**, *17*, 1194–1200. [[CrossRef](#)]
19. Khushaim, M.; Alamri, S.; Kattan, N.; Jaber, A.; Alamri, S. Study of Kesterite Cu<sub>2</sub>ZnSnS<sub>4</sub> (CZTS) Thin Films Deposited by Spray Technique for Photovoltaic Applications. *J. Taibah Univ. Sci.* **2021**, *15*, 329–339. [[CrossRef](#)]
20. Ahmoum, H.; Chelvanathan, P.; Su'ait, M.S.; Boughrara, M.; Li, G.; Al-Waeli, A.H.A.; Sopian, K.; Kerouad, M.; Amin, N. Impact of Preheating Environment on Microstructural and Optoelectronic Properties of Cu<sub>2</sub>ZnSnS<sub>4</sub> (CZTS) Thin Films Deposited by Spin-Coating. *Superlattices Microstruct.* **2020**, *140*, 106452. [[CrossRef](#)]
21. Chaudhari, S.; Kannan, P.K.; Dey, S.R. Influence of Stabilizing Agent on Dip Coating of Cu<sub>2</sub>ZnSnS<sub>4</sub> Thin Film. *Thin Solid. Films* **2017**, *636*, 144–149. [[CrossRef](#)]
22. Ahmad, A.A.; Migdadi, A.B.; Alsaad, A.M.; Qattan, I.A.; Al-Bataineh, Q.M.; Telfah, A. Computational and Experimental Characterizations of Annealed Cu<sub>2</sub>ZnSnS<sub>4</sub> Thin Films. *Heliyon* **2021**, *8*, e08683. [[CrossRef](#)]
23. Shaikh, R.A.G.; More, S.A.; Bisen, G.G.; Ghosh, S.S. Study the Properties of Solution Processable CZTS Thin Films Induced by Annealing Treatment: Study of Annealing Time. *Semiconductors* **2020**, *54*, 1011–1015. [[CrossRef](#)]
24. Aabel, P.; Anupama, A.; Kumar, M.C.S. Preparation and Characterization of CZTS Thin Films by Vacuum-Assisted Spray Pyrolysis and Fabrication of Cd-Free Heterojunction Solar Cells. *Semicond. Sci. Technol.* **2023**, *38*, 045010. [[CrossRef](#)]

25. Diwate, K.; Mohite, K.; Shinde, M.; Rondiya, S.; Pawbake, A.; Date, A.; Pathan, H.; Jadkar, S. Synthesis and Characterization of Chemical Spray Pyrolysed CZTS Thin Films for Solar Cell Applications. *Energy Procedia* **2017**, *110*, 180–187. [[CrossRef](#)]
26. Kumar, Y.B.K.; Babu, G.S.; Bhaskar, P.U.; Raja, V.S. Effect of Starting-solution pH on the Growth of  $\text{Cu}_2\text{ZnSnS}_4$  Thin Films Deposited by Spray Pyrolysis. *Physica Status Solidi* **2009**, *206*, 1525–1530. [[CrossRef](#)]
27. Shamardin, A.; Kurbatov, D.; Grase, L.; Vecstaudža, J.; Kaupužs, J.; Medvids, A. Quality Improvement of CZTS Thin Films Deposited by Spray Pyrolysis Method Using Pulsed Nd: YAG Laser Irradiation. *Appl. Surf. Sci.* **2019**, *488*, 827–835. [[CrossRef](#)]
28. Kamoun, N.; Bouzouita, H.; Rezig, B. Fabrication and Characterization of  $\text{Cu}_2\text{ZnSnS}_4$  Thin Films Deposited by Spray Pyrolysis Technique. *Thin Solid. Films* **2007**, *515*, 5949–5952. [[CrossRef](#)]
29. Vauche, L.; Dubois, J.; Laparre, A.; Pasquinelli, M.; Bodnar, S.; Grand, P.-P.; Jaime, S. Rapid Thermal Processing Annealing Challenges for Large Scale  $\text{Cu}_2\text{ZnSnS}_4$  Thin Films. *Phys. Status Solidi A* **2015**, *212*, 103–108. [[CrossRef](#)]
30. Jung, S.; Gwak, J.; Yun, J.H.; Ahn, S.; Nam, D.; Cheong, H.; Ahn, S.; Cho, A.; Shin, K.; Yoon, K.  $\text{Cu}_2\text{ZnSnSe}_4$  Thin Film Solar Cells Based on a Single-Step Co-Evaporation Process. *Thin Solid. Films* **2013**, *535*, 52–56. [[CrossRef](#)]
31. Zhi, Z.; Wang, S.; Huang, L.; Li, J.; Xiao, X. Fabrication of CZTS Thin Films and Solar Cells via Single-Step Co-Evaporation Method. *Mater. Sci. Semicond. Process.* **2022**, *144*, 106592. [[CrossRef](#)]
32. Zhang, L.; Karthikeyan, S.; Sibakoti, M.J.; Campbell, S.A.  $\text{Cu}_2\text{ZnSnS}_4$  Thin Film Growth Optimization and Post Rapid Thermal Annealing of Solar Cells and Its Influence on Device Performance. In Proceedings of the 2015 IEEE 42nd Photovoltaic Specialist Conference (PVSC), New Orleans, LA, USA, 14–19 June 2015; pp. 1–6.
33. Choudhari, N.J.; George, S.D.; Raviprakash, Y. Influence of Sulfurization Time and Cu-ZnS-Sn Stack Order on the Properties of Thermally Evaporated CZTS Thin Films. *J. Mater. Sci. Mater. Electron.* **2022**, *33*, 5341–5350. [[CrossRef](#)]
34. Tao, S.; Dong, L.; Han, J.; Wang, Y.; Gong, Q.; Wei, J.; Zhao, M.; Zhuang, D. Efficiency Enhancement of CZTSe Solar Cells Based on in Situ K-Doped Precursor. *J. Mater. Chem. A* **2023**, *11*, 9085–9096. [[CrossRef](#)]
35. Ogugua, S.N.; Ntwaeaborwa, O.M.; Swart, H.C. Latest Development on Pulsed Laser Deposited Thin Films for Advanced Luminescence Applications. *Coatings* **2020**, *10*, 1078. [[CrossRef](#)]
36. Oulad Elhmaidi, Z.; Abd-Lefdil, M.; El Khakani, M.A. Photoconversion Optimization of Pulsed-Laser-Deposited p-CZTS/n-Si-Nanowires Heterojunction-Based Photovoltaic Devices. *Nanomaterials* **2020**, *10*, 1393. [[CrossRef](#)]
37. Vanalakar, S.A.; Agawane, G.L.; Shin, S.W.; Suryawanshi, M.P.; Gurav, K.V.; Jeon, K.S.; Patil, P.S.; Jeong, C.W.; Kim, J.Y.; Kim, J.H. A Review on Pulsed Laser Deposited CZTS Thin Films for Solar Cell Applications. *J. Alloys Compd.* **2015**, *619*, 109–121. [[CrossRef](#)]
38. Cazzaniga, A.; Crovetto, A.; Yan, C.; Sun, K.; Hao, X.; Ramis Estelrich, J.; Canulescu, S.; Stamate, E.; Pryds, N.; Hansen, O.; et al. Ultra-Thin  $\text{Cu}_2\text{ZnSnS}_4$  Solar Cell by Pulsed Laser Deposition. *Sol. Energy Mater. Sol. Cells* **2017**, *166*, 91–99. [[CrossRef](#)]
39. Ettliger, R.B.; Crovetto, A.; Canulescu, S.; Cazzaniga, A.; Ravnkilde, L.; Youngman, T.; Hansen, O.; Pryds, N.; Schou, J. Formation of Copper Tin Sulfide Films by Pulsed Laser Deposition at 248 and 355 Nm. *Appl. Phys. A* **2016**, *122*, 466. [[CrossRef](#)]
40. Cazzaniga, A.; Ettliger, R.B.; Canulescu, S.; Schou, J.; Pryds, N. Nanosecond Laser Ablation and Deposition of Silver, Copper, Zinc and Tin. *Appl. Phys. A* **2014**, *117*, 89–92. [[CrossRef](#)]
41. Noroozi, M.; Petruhins, A.; Greczynski, G.; Rosen, J.; Eklund, P. Structural and Mechanical Properties of Amorphous AlMgB14 Thin Films Deposited by DC Magnetron Sputtering on Si,  $\text{Al}_2\text{O}_3$  and MgO Substrates. *Appl. Phys. A* **2020**, *126*, 133. [[CrossRef](#)]
42. Olgar, M.A.; Klaer, J.; Mainz, R.; Levenco, S.; Just, J.; Bacaksiz, E.; Unold, T. Effect of Precursor Stacking Order and Sulfurization Temperature on Compositional Homogeneity of CZTS Thin Films. *Thin Solid. Films* **2016**, *615*, 402–408. [[CrossRef](#)]
43. Jheng, B.-T.; Liu, P.-T.; Wu, M.-C. A Promising Sputtering Route for Dense  $\text{Cu}_2\text{ZnSnS}_4$  Absorber Films and Their Photovoltaic Performance. *Sol. Energy Mater. Sol. Cells* **2014**, *128*, 275–282. [[CrossRef](#)]
44. Xie, M.; Zhuang, D.; Zhao, M.; Zhuang, Z.; Ouyang, L.; Li, X.; Song, J. Preparation and Characterization of  $\text{Cu}_2\text{ZnSnS}_4$  Thin Films and Solar Cells Fabricated from Quaternary Cu-Zn-Sn-S Target. *Int. J. Photoenergy* **2013**, *2013*, 1–9. [[CrossRef](#)]
45. Olgar, M.A.; Klaer, J.; Mainz, R.; Ozyuzer, L.; Unold, T.  $\text{Cu}_2\text{ZnSnS}_4$ -Based Thin Films and Solar Cells by Rapid Thermal Annealing Processing. *Thin Solid. Films* **2017**, *628*, 1–6. [[CrossRef](#)]
46. Behera, N.; Mohan, D.B. The Phase Optimization, Optical and Electrical Properties of Kesterite  $\text{Cu}_2\text{ZnSnS}_4$  Thin Film Prepared by Single Target RF Magnetron Sputtering Technique for Solar Cell Application. *Mater. Res. Express* **2020**, *6*, 126457. [[CrossRef](#)]
47. Zhao, L.; Fei, F.Y.; Wang, J.; Wang, F.; Wang, C.; Li, J.; Wang, J.; Cheng, Z.; Dou, S.; Wang, X. Improvement of Thermoelectric Properties and Their Correlations with Electron Effective Mass in  $\text{Cu}_{1.985}\text{SxSe}_{1-x}$ . *Sci. Rep.* **2017**, *7*, 40436. [[CrossRef](#)]
48. Khalkar, A.; Lim, K.-S.; Yu, S.-M.; Patole, S.P.; Yoo, J.-B. Deposition of  $\text{Cu}_2\text{ZnSnS}_4$  Thin Films by Magnetron Sputtering and Subsequent Sulphurization. *Electron. Mater. Lett.* **2014**, *10*, 43–49. [[CrossRef](#)]
49. Gudmundsson, J.T. Physics and Technology of Magnetron Sputtering Discharges. *Plasma Sources Sci. Technol.* **2020**, *29*, 113001. [[CrossRef](#)]
50. Alvarez, R.; Garcia-Valenzuela, A.; Lopez-Santos, C.; Ferrer, F.J.; Rico, V.; Guillen, E.; Alcon-Camas, M.; Escobar-Galindo, R.; Gonzalez-Elipse, A.R.; Palmero, A. High-Rate Deposition of Stoichiometric Compounds by Reactive Magnetron Sputtering at Oblique Angles. *Plasma Process. Polym.* **2016**, *13*, 960–964. [[CrossRef](#)]
51. Vishwakarma, M.; Karakulina, O.M.; Abakumov, A.M.; Hadermann, J.; Mehta, B.R. Nanoscale Characterization of Growth of Secondary Phases in Off-Stoichiometric CZTS Thin Films. *J. Nanosci. Nanotechnol.* **2018**, *18*, 1688–1695. [[CrossRef](#)]
52. Sava, F.; Diagne, O.; Galca, A.-C.; Simandan, I.-D.; Matei, E.; Burdusel, M.; Becherescu, N.; Becherescu, V.; Mihai, C.; Velea, A. Secondary Crystalline Phases Influence on Optical Properties in Off-Stoichiometric  $\text{Cu}_2\text{S}-\text{ZnS}-\text{SnS}_2$  Thin Films. *Materials* **2020**, *13*, 4624. [[CrossRef](#)]

53. Hartman, K.; Newman, B.K.; Johnson, J.L.; Du, H.; Fernandes, P.A.; Chawla, V.; Bolin, T.; Clemens, B.M.; Da Cunha, A.F.; Teeter, G.; et al. Detection of ZnS Phases in CZTS Thin-Films by EXAFS. In Proceedings of the 2011 37th IEEE Photovoltaic Specialists Conference, Seattle, WA, USA, 19–24 June 2011; pp. 2506–2509.
54. Agrawal, S.; De Souza, D.O.; Balasubramanian, C.; Mukherjee, S. Effect of Secondary Phases Controlled by Precursor Composition on the Efficiency of CZTS Thin Film Solar Cell. *Sol. Energy Mater. Sol. Cells* **2024**, *267*, 112719. [[CrossRef](#)]
55. Raiguru, J.; Subramanyam, B.; Sa, K.; Alam, I.; Das, S.; Mukherjee, J.; Mahakul, P.C.; Subudhi, B.; Mahanandia, P. Impact of Annealing Temperature on the Phase of CZTS with the Variation in Surface Morphological Changes and Extraction of Optical Bandgap. *IOP Conf. Ser. Mater. Sci. Eng.* **2017**, *178*, 012017. [[CrossRef](#)]
56. Ashfaq, A.; Jacob, J.; Bano, N.; Nabi, M.A.U.; Ali, A.; Ahmad, W.; Mahmood, K.; Arshad, M.I.; Ikram, S.; Rehman, U.; et al. A Two Step Technique to Remove the Secondary Phases in CZTS Thin Films Grown by Sol-Gel Method. *Ceram. Int.* **2019**, *45*, 10876–10881. [[CrossRef](#)]
57. Chen, G.; Wang, W.; Zhang, J.; Chen, S.; Huang, Z. Formation Mechanism of Secondary Phases in  $\text{Cu}_2\text{ZnSnS}_4$  Growth under Different Copper Content. *Mater. Lett.* **2017**, *186*, 98–101. [[CrossRef](#)]
58. Stanchik, A.V.; Tivanov, M.S.; Tyukhov, I.I.; Juskenas, R.; Korolik, O.V.; Gremenok, V.F.; Saad, A.M.; Naujokaitis, A. Temperature Dependence of Raman Scattering in the  $\text{Cu}_2\text{ZnSnSe}_4$  Thin Films on a Ta Foil Substrate. *Sol. Energy* **2020**, *201*, 480–488. [[CrossRef](#)]
59. Vishwakarma, M.; Agrawal, K.; Hadermann, J.; Mehta, B.R. Investigating the Effect of Sulphurization on Volatility of Compositions in Cu-Poor and Sn-Rich CZTS Thin Films. *Appl. Surf. Sci.* **2020**, *507*, 145043. [[CrossRef](#)]
60. Redinger, A.; Hönes, K.; Fontané, X.; Izquierdo-Roca, V.; Saucedo, E.; Valle, N.; Pérez-Rodríguez, A.; Siebentritt, S. Detection of a ZnSe Secondary Phase in Coevaporated  $\text{Cu}_2\text{ZnSnSe}_4$  Thin Films. *Appl. Phys. Lett.* **2011**, *98*, 101907. [[CrossRef](#)]
61. Ghediya, P.R.; Chaudhuri, T.K. Microwave-Processed Copper Zinc Tin Sulphide (CZTS) Inks for Coatings in Solar Cells. In *Advanced Ceramic and Metallic Coating and Thin Film Materials for Energy and Environmental Applications*; Zhang, J., Jung, Y.-G., Eds.; Springer International Publishing: Cham, Switzerland, 2018; pp. 121–174, ISBN 978-3-319-59905-2.
62. Jiang, M.; Yan, X.  $\text{Cu}_2\text{ZnSnS}_4$  Thin Film Solar Cells: Present Status and Future Prospects. In *Solar Cells-Research and Application Perspectives*; Morales-Acevedo, A., Ed.; InTech: Rijeka, Croatia, 2013; ISBN 978-953-51-1003-3.
63. Shi, Z.; Attygalle, D.; Jayatissa, A.H. Kesterite-Based next Generation High Performance Thin Film Solar Cell: Current Progress and Future Prospects. *J. Mater. Sci. Mater. Electron.* **2017**, *28*, 2290–2306. [[CrossRef](#)]
64. Berg, D.M.; Arasimowicz, M.; Djemour, R.; Gütay, L.; Siebentritt, S.; Schorr, S.; Fontané, X.; Izquierdo-Roca, V.; Pérez-Rodríguez, A.; Dale, P.J. Discrimination and Detection Limits of Secondary Phases in  $\text{Cu}_2\text{ZnSnS}_4$  Using X-Ray Diffraction and Raman Spectroscopy. *Thin Solid. Films* **2014**, *569*, 113–123. [[CrossRef](#)]
65. Zaki, M.Y.; Sava, F.; Simandan, I.-D.; Buruiana, A.T.; Stavarache, I.; Bocirnea, A.E.; Mihai, C.; Velea, A.; Galca, A.-C. A Two-Step Magnetron Sputtering Approach for the Synthesis of  $\text{Cu}_2\text{ZnSnS}_4$  Films from  $\text{Cu}_2\text{SnS}_3/\text{ZnS}$  Stacks. *ACS Omega* **2022**, *7*, 23800–23814. [[CrossRef](#)]
66. Tanaka, T.; Sueishi, T.; Saito, K.; Guo, Q.; Nishio, M.; Yu, K.M.; Walukiewicz, W. Existence and Removal of  $\text{Cu}_2\text{Se}$  Second Phase in Coevaporated  $\text{Cu}_2\text{ZnSnSe}_4$  Thin Films. *J. Appl. Phys.* **2012**, *111*, 053522. [[CrossRef](#)]
67. Zaki, M.Y.; Sava, F.; Simandan, I.D.; Buruiana, A.T.; Mihai, C.; Velea, A.; Galca, A.C.  $\text{Cu}_2\text{SnSe}_3$  Phase Formation from Different Metallic and Binary Chalcogenides Stacks Using Magnetron Sputtering. *Mater. Sci. Semicond. Process.* **2023**, *153*, 107195. [[CrossRef](#)]
68. Salomé, P.M.P.; Fernandes, P.A.; Leitão, J.P.; Sousa, M.G.; Teixeira, J.P.; da Cunha, A.F. Secondary Crystalline Phases Identification in  $\text{Cu}_2\text{ZnSnSe}_4$  Thin Films: Contributions from Raman Scattering and Photoluminescence. *J. Mater. Sci.* **2014**, *49*, 7425–7436. [[CrossRef](#)]
69. Catana, D.-S.; Zaki, M.Y.; Simandan, I.-D.; Buruiana, A.-T.; Sava, F.; Velea, A. Understanding the Effects of Post-Deposition Sequential Annealing on the Physical and Chemical Properties of  $\text{Cu}_2\text{ZnSnSe}_4$  Thin Films. *Surfaces* **2023**, *6*, 466–479. [[CrossRef](#)]
70. Dimitrievska, M.; Xie, H.; Fairbrother, A.; Fontané, X.; Gurieva, G.; Saucedo, E.; Pérez-Rodríguez, A.; Schorr, S.; Izquierdo-Roca, V. Multiwavelength Excitation Raman Scattering of  $\text{Cu}_2\text{ZnSn}(\text{S}_x\text{Se}_{1-x})_4$  ( $0 \leq x \leq 1$ ) Polycrystalline Thin Films: Vibrational Properties of Sulfoselenide Solid Solutions. *Appl. Phys. Lett.* **2014**, *105*, 031913. [[CrossRef](#)]
71. Dimitrievska, M.; Boero, F.; Litvinchuk, A.P.; Delsante, S.; Borzone, G.; Perez-Rodríguez, A.; Izquierdo-Roca, V. Structural Polymorphism in “Kesterite”  $\text{Cu}_2\text{ZnSnS}_4$ : Raman Spectroscopy and First-Principles Calculations Analysis. *Inorg. Chem.* **2017**, *56*, 3467–3474. [[CrossRef](#)]
72. Fernandes, P.A.; Salomé, P.M.P.; da Cunha, A.F. A Study of Ternary  $\text{Cu}_2\text{SnS}_3$  and  $\text{Cu}_3\text{SnS}_4$  Thin Films Prepared by Sulfurizing Stacked Metal Precursors. *J. Phys. D Appl. Phys.* **2010**, *43*, 215403. [[CrossRef](#)]
73. Avellaneda, D.; Paul, A.; Shaji, S.; Krishnan, B. Synthesis of  $\text{Cu}_2\text{SnS}_3$ ,  $\text{Cu}_3\text{SnS}_4$ , and  $\text{Cu}_4\text{SnS}_4$  Thin Films by Sulfurization of SnS-Cu Layers at a Selected Temperature and /or Cu Layers Thickness. *J. Solid. State Chem.* **2022**, *306*, 122711. [[CrossRef](#)]
74. Gang, M.G.; Gurav, K.V.; Shin, S.W.; Hong, C.W.; Min, J.H.; Suryawanshi, M.P.; Vanalakar, S.A.; Lee, D.S.; Kim, J.H. A 5.1% Efficient Kesterite  $\text{Cu}_2\text{ZnSnS}_4$  (CZTS) Thin Film Solar Cell Prepared Using Modified Sulfurization Process. *Phys. Status Solidi (C) Curr. Top. Solid. State Phys.* **2015**, *12*, 713–716. [[CrossRef](#)]
75. Patel, K.; Kheraj, V.; Shah, D.V.; Panchal, C.J.; Dhere, N.G.  $\text{Cu}_2\text{ZnSnS}_4$  Thin-Films Grown by Dip-Coating: Effects of Annealing. *J. Alloys Compd.* **2016**, *663*, 842–847. [[CrossRef](#)]
76. Zaki, M.Y.; Sava, F.; Simandan, I.D.; Buruiana, A.T.; Mihai, C.; Velea, A.; Galca, A.C. Effect of the Stacking Order, Annealing Temperature and Atmosphere on Crystal Phase and Optical Properties of  $\text{Cu}_2\text{SnS}_3$ . *Sci. Rep.* **2022**, *12*, 7958. [[CrossRef](#)]

77. Tian, G.; Huang, C.; Luo, X.; Zhao, Z.; Peng, Y.; Gao, Y.; Tang, N.; Dsoke, S. Study of the Lithium Storage Mechanism of N-Doped Carbon-Modified  $\text{Cu}_2\text{S}$  Electrodes for Lithium-Ion Batteries. *Chem. A Eur. J.* **2021**, *27*, 13774–13782. [[CrossRef](#)]
78. Lund, E.A.; Du, H.; Hlaing OO, W.M.; Teeter, G.; Scarpulla, M.A. Investigation of Combinatorial Coevaporated Thin Film  $\text{Cu}_2\text{ZnSnS}_4$  (II): Beneficial Cation Arrangement in Cu-Rich Growth. *J. Appl. Phys.* **2014**, *115*, 173503. [[CrossRef](#)]
79. Gong, X.; Yan, T.; Li, J.; Liu, J.; Zou, H.; Zhang, B.; Wu, H.; Zhou, Z.; Zhou, X. Revealing the Anisotropic Phonon Behaviours of Layered SnS by Angle/Temperature-Dependent Raman Spectroscopy. *RSC Adv.* **2022**, *12*, 32262–32269. [[CrossRef](#)]
80. Raadik, T.; Grossberg, M.; Krustok, J.; Kauk-Kuusik, M.; Crovetto, A.; Bolt Ettliger, R.; Hansen, O.; Schou, J. Temperature Dependent Photoreflectance Study of  $\text{Cu}_2\text{SnS}_3$  Thin Films Produced by Pulsed Laser Deposition. *Appl. Phys. Lett.* **2017**, *110*, 261105. [[CrossRef](#)]
81. Ahmet, I.Y.; Hill, M.S.; Johnson, A.L.; Peter, L.M. Polymorph-Selective Deposition of High Purity SnS Thin Films from a Single Source Precursor. *Chem. Mater.* **2015**, *27*, 7680–7688. [[CrossRef](#)]
82. Skelton, J.M.; Burton, L.A.; Jackson, A.J.; Oba, F.; Parker, S.C.; Walsh, A. Lattice Dynamics of the Tin Sulphides  $\text{SnS}_2$ , SnS and  $\text{Sn}_2\text{S}_3$ : Vibrational Spectra and Thermal Transport. *Phys. Chem. Chem. Phys.* **2017**, *19*, 12452–12465. [[CrossRef](#)]
83. Zhang, K.; Su, Z.; Zhao, L.; Yan, C.; Liu, F.; Cui, H.; Hao, X.; Liu, Y. Improving the Conversion Efficiency of  $\text{Cu}_2\text{ZnSnS}_4$  Solar Cell by Low Pressure Sulfurization. *Appl. Phys. Lett.* **2014**, *104*, 141101. [[CrossRef](#)]
84. Alvarez Barragan, A.; Malekpour, H.; Exarhos, S.; Balandin, A.A.; Mangolini, L. Grain-to-Grain Compositional Variations and Phase Segregation in Copper–Zinc–Tin–Sulfide Films. *ACS Appl. Mater. Interfaces* **2016**, *8*, 22971–22976. [[CrossRef](#)]
85. Babichuk, I.S.; Semenenko, M.O.; Caballero, R.; Datsenko, O.I.; Golovynskyi, S.; Qiu, R.; Huang, C.; Hu, R.; Babichuk, I.V.; Ziniuk, R.R.; et al. Raman Mapping of  $\text{MoS}_2$  at  $\text{Cu}_2\text{ZnSnS}_4$ /Mo Interface in Thin Film. *Sol. Energy* **2020**, *205*, 154–160. [[CrossRef](#)]
86. Huang, S.; Liang, L.; Ling, X.; Puzetzy, A.A.; Geohegan, D.B.; Sumpter, B.G.; Kong, J.; Meunier, V.; Dresselhaus, M.S. Low-Frequency Interlayer Raman Modes to Probe Interface of Twisted Bilayer  $\text{MoS}_2$ . *Nano Lett.* **2016**, *16*, 1435–1444. [[CrossRef](#)] [[PubMed](#)]
87. Zaki, M.Y.; Sava, F.; Simandan, I.D.; Buruiana, A.T.; Bocirnea, A.E.; Stavarache, I.; Velea, A.; Galca, A.C.; Pintilie, L. From Non-Stoichiometric CTSe to Single Phase and Stoichiometric CZTSe Films by Annealing under Sn+Se Atmosphere. *Ceram. Int.* **2023**, *49*, 33692–33702. [[CrossRef](#)]
88. Dimitrievska, M.; Oliva, F.; Guc, M.; Giraldo, S.; Saucedo, E.; Pérez-Rodríguez, A.; Izquierdo-Roca, V. Defect Characterisation in  $\text{Cu}_2\text{ZnSnSe}_4$  Kesterites via Resonance Raman Spectroscopy and the Impact on Optoelectronic Solar Cell Properties. *J. Mater. Chem. A* **2019**, *7*, 13293–13304. [[CrossRef](#)]
89. Ahmadi, M.; Pramana, S.S.; Batabyal, S.K.; Boothroyd, C.; Mhaisalkar, S.G.; Lam, Y.M. Synthesis of  $\text{Cu}_2\text{SnSe}_3$  Nanocrystals for Solution Processable Photovoltaic Cells. *Inorg. Chem.* **2013**, *52*, 1722–1728. [[CrossRef](#)] [[PubMed](#)]
90. Altosaar, M.; Raudoja, J.; Timmo, K.; Danilson, M.; Grossberg, M.; Krustok, J.; Mellikov, E.  $\text{Cu}_2\text{Zn}_{1-x}\text{Cd}_x\text{Sn}(\text{Se}_{1-y}\text{S}_y)_4$  Solid Solutions as Absorber Materials for Solar Cells. *Phys. Status Solidi* **2008**, *205*, 167–170. [[CrossRef](#)]
91. Shitu, I.G.; Liew, J.Y.C.; Talib, Z.A.; Baqiah, H.; Awang Kechik, M.M.; Ahmad Kamarudin, M.; Osman, N.H.; Low, Y.J.; Lakin, I.I. Influence of Irradiation Time on the Structural and Optical Characteristics of CuSe Nanoparticles Synthesized via Microwave-Assisted Technique. *ACS Omega* **2021**, *6*, 10698–10708. [[CrossRef](#)] [[PubMed](#)]
92. Juškėnas, R.; Mockus, Z.; Giraitis, R.; Selskis, A.; Stalnionis, G.; Kanapekaitė, S.; Drabavičius, A.; Kalinauskas, P.; Niaura, G. Structural and Photoelectrochemical Characterization of  $\text{Cu}_2\text{SnSe}_3$  Thin Films Fabricated by Electrochemical Co-Deposition and Selenization. *J. Alloys Compd.* **2018**, *767*, 345–352. [[CrossRef](#)]
93. Gurieva, G.; Levcenco, S.; Pereira Correia de Sousa, A.; Unold, T.; Schorr, S. Investigation of Detection Limits of ZnSe and  $\text{Cu}_2\text{SnSe}_3$  Secondary Phases in  $\text{Cu}_2\text{ZnSnSe}_4$ . *Phys. Status Solidi C* **2017**, *14*, 1700166.
94. Nam, D.; Lee, J.-U.; Cheong, H. Excitation Energy Dependent Raman Spectrum of  $\text{MoSe}_2$ . *Sci. Rep.* **2015**, *5*, 17113. [[CrossRef](#)]
95. Ismail, A.; Cho, J.W.; Park, S.J.; Hwang, Y.J.; Min, B.K. Synthesis of Solution-Processed  $\text{Cu}_2\text{ZnSnSe}_4$  Thin Films on Transparent Conducting Oxide Glass Substrates. *Bull. Korean Chem. Soc.* **2014**, *35*, 1985–1988. [[CrossRef](#)]
96. Just, J.; Sutter-Fella, C.M.; Lützenkirchen-Hecht, D.; Frahm, R.; Schorr, S.; Unold, T. Secondary Phases and Their Influence on the Composition of the Kesterite Phase in CZTS and CZTSe Thin Films. *Phys. Chem. Chem. Phys.* **2016**, *18*, 15988–15994. [[CrossRef](#)] [[PubMed](#)]
97. Rudisch, K.; Davydova, A.; Riekehr, L.; Adolfsson, J.; Quaglia Casal, L.; Platzer-Björkman, C.; Scragg, J. Prospects for Defect Engineering in  $\text{Cu}_2\text{ZnSnS}_4$  Solar Absorber Films. *J. Mater. Chem. A* **2020**, *8*, 15864–15874. [[CrossRef](#)]
98. Abusnina, M.; Matin, M.; Moutinho, H.R.; Blackburn, J.L.; Alleman, J.; DeHart, C.; To, B.; Al-Jassim, M. Suppression of the  $\text{Cu}_{2-x}\text{S}$  Secondary Phases in CZTS Films Through Controlling the Film Elemental Composition. *IEEE J. Photovolt.* **2015**, *5*, 1470–1475. [[CrossRef](#)]
99. Kalinauskas, P.; Norkus, E.; Mockus, Z.; Giraitis, R.; Stalnionis, G.; Jasulaitiene, V.; Juškėnas, R. The Influence of Removal of Secondary Phases and Dissolution By-Product from the Surface of  $\text{Cu}_2\text{ZnSnS}_4$  Film on the Photoelectrochemical Response of This Film. *J. Electrochem. Soc.* **2020**, *167*, 026513. [[CrossRef](#)]
100. Yu, S.M.; Lim, K.-S.; Shin, D.-W.; Oh, T.-S.; Yoo, J.-B. Effect of the Intermediate Sulfide Layer on the  $\text{Cu}_2\text{ZnSnS}_4$ -Based Solar Cells. *J. Mater. Sci. Mater. Electron.* **2017**, *28*, 5696–5702. [[CrossRef](#)]
101. Li, W.; Chen, J.; Yan, C.; Liu, F.; Hao, X. Transmission Electron Microscopy Analysis for the Process of Crystallization of  $\text{Cu}_2\text{ZnSnS}_4$  Film from Sputtered Zn/CuSn Precursor. *Nanotechnology* **2014**, *25*, 195701. [[CrossRef](#)] [[PubMed](#)]

102. Buffière, M.; Brammertz, G.; Batuk, M.; Verbist, C.; Mangin, D.; Koble, C.; Hadermann, J.; Meuris, M.; Poortmans, J. Microstructural Analysis of 9.7% Efficient  $\text{Cu}_2\text{ZnSnSe}_4$  Thin Film Solar Cells. *Appl. Phys. Lett.* **2014**, *105*, 183903. [[CrossRef](#)]
103. Fella, C.M.; Uhl, A.R.; Romanyuk, Y.E.; Tiwari, A.N.  $\text{Cu}_2\text{ZnSnSe}_4$  Absorbers Processed from Solution Deposited Metal Salt Precursors under Different Selenization Conditions. *Physica Status Solidi* **2012**, *209*, 1043–1048. [[CrossRef](#)]
104. Scragg, J.J.; Kubart, T.; Wätjen, J.T.; Ericson, T.; Linnarsson, M.K.; Platzer-Björkman, C. Effects of Back Contact Instability on  $\text{Cu}_2\text{ZnSnS}_4$  Devices and Processes. *Chem. Mater.* **2013**, *25*, 3162–3171. [[CrossRef](#)]
105. Bishop, D.M.; McCandless, B.E.; Mangan, T.C.; Dobson, K.; Birkmire, R. Effects of Growth Conditions on Secondary Phases in CZTSe Thin Films Deposited by Co-Evaporation. *MRS Proc.* **2013**, *1538*, 75–82. [[CrossRef](#)]
106. Li, W. The Effect of ZnS Segregation on Zn-Rich CZTS Thin Film Solar Cells. *J. Alloys Compd.* **2015**, *632*, 178–184. [[CrossRef](#)]
107. Huang, L.; Wang, S.; Zhong, L.; Chen, L.; Xiao, X. Role of ZnS Particles in the Performance of  $\text{Cu}_2\text{ZnSnS}_4$  Thin Film Solar Cells: A Comparative Study by Active Control of Zinc Deposition in Coevaporated Precursors. *Solar RRL* **2020**, *4*, 2000334. [[CrossRef](#)]
108. Lai, F.-I.; Yang, J.-F.; Hsu, Y.-C.; Kuo, S.-Y. Suppressing the Formation of Double-Layer in  $\text{Cu}_2\text{ZnSnSe}_4$ (CZTSe) Absorber Layer by Facile Heating Process through Nontoxic Selenium Atmosphere. *Int. J. Energy Res.* **2022**, *46*, 3686–3696. [[CrossRef](#)]
109. Wang, W.; Chen, G.; Cai, H.; Chen, B.; Yao, L.; Yang, M.; Chen, S.; Huang, Z. The Effects of  $\text{SnS}_2$  Secondary Phases on  $\text{Cu}_2\text{ZnSnS}_4$  Solar Cells: A Promising Mechanical Exfoliation Method for Its Removal. *J. Mater. Chem. A* **2018**, *6*, 2995–3004. [[CrossRef](#)]
110. Engberg, S.; Symonowicz, J.; Schou, J.; Canulescu, S.; Jensen, K.M.Ø. Characterization of  $\text{Cu}_2\text{ZnSnS}_4$  Particles Obtained by the Hot-Injection Method. *ACS Omega* **2020**, *5*, 10501–10509. [[CrossRef](#)]
111. Lin, Y.-C.; Su, Z.-Y. Tin–Selenium Secondary Phase Etching of  $\text{Cu}_2\text{ZnSnSe}_4$ : A Selective Removal Route To Improve Solar Cell Efficiency. *ACS Appl. Energy Mater.* **2018**, *1*, 6725–6729. [[CrossRef](#)]
112. Temgoua, S.; Bodeux, R.; Naghavi, N.; Delbos, S. Effects of  $\text{SnSe}_2$  Secondary Phases on the Efficiency of  $\text{Cu}_2\text{ZnSn}(\text{S}_x\text{Se}_{1-x})_4$  Based Solar Cells. *Thin Solid. Films* **2015**, *582*, 215–219. [[CrossRef](#)]
113. Becerril-Romero, I.; Acebo, L.; Oliva, F.; Izquierdo-Roca, V.; López-Marino, S.; Espíndola-Rodríguez, M.; Neuschitzer, M.; Sánchez, Y.; Placidi, M.; Pérez-Rodríguez, A.; et al. C ZTS e Solar Cells Developed on Polymer Substrates: Effects of Low-temperature Processing. *Progress. Photovolt.* **2018**, *26*, 55–68. [[CrossRef](#)]
114. Guo, L.; Zhu, Y.; Gunawan, O.; Gokmen, T.; Deline, V.R.; Ahmed, S.; Romankiw, L.T.; Deligianni, H. Electrodeposited  $\text{Cu}_2\text{ZnSnSe}_4$  Thin Film Solar Cell with 7% Power Conversion Efficiency. *Progress. Photovolt.* **2014**, *22*, 58–68. [[CrossRef](#)]
115. Chen, W.; Taskesen, T.; Nowak, D.; Mikolajczak, U.; Sayed, M.H.; Pareek, D.; Ohland, J.; Schnabel, T.; Ahlswede, E.; Hauschild, D.; et al. Modifications of the CZTSe/Mo Back-Contact Interface by Plasma Treatments. *RSC Adv.* **2019**, *9*, 26850–26855. [[CrossRef](#)]
116. Lu, X.; Xu, B.; Qin, X.; Chen, Y.; Yang, P.; Chu, J.; Sun, L. Modification of Back Contact in  $\text{Cu}_2\text{ZnSnS}_4$  Solar Cell by Inserting Al-Doped ZnO Intermediate Layer. *ACS Appl. Mater. Interfaces* **2020**, *12*, 58060–58071. [[CrossRef](#)]
117. Gunavathy, K.V.; Tamilarasan, K.; Rangasami, C.; Arulanantham, A.M.S. A Review on Growth Optimization of Spray Pyrolyzed  $\text{Cu}_2\text{ZnSnS}_4$  Chalcogenide Absorber Thin Film. *Int. J. Energy Res.* **2019**, *43*, 7716–7754. [[CrossRef](#)]
118. Tao, J.; Liu, J.; Chen, L.; Cao, H.; Meng, X.; Zhang, Y.; Zhang, C.; Sun, L.; Yang, P.; Chu, J. 7.1% Efficient Co-Electroplated  $\text{Cu}_2\text{ZnSnS}_4$  Thin Film Solar Cells with Sputtered CdS Buffer Layers. *Green. Chem.* **2016**, *18*, 550–557. [[CrossRef](#)]
119. Simya, O.K.; Geetha Priyadarshini, B.; Balachander, K.; Ashok, A.M. Formation of a Phase Pure Kesterite CZTSe Thin Films Using Multisource Hybrid Physical Vapour Deposition. *Mater. Res. Express* **2020**, *7*, 016419. [[CrossRef](#)]
120. Gang, M.G.; Shin, S.W.; Hong, C.W.; Gurav, K.V.; Gwak, J.; Yun, J.H.; Lee, J.Y.; Kim, J.H. Sputtering Processed Highly Efficient  $\text{Cu}_2\text{ZnSn}(\text{S,Se})_4$  Solar Cells by a Low-Cost, Simple, Environmentally Friendly, and up-Scalable Strategy. *Green. Chem.* **2016**, *18*, 700–711. [[CrossRef](#)]
121. Olgar, M.A. Optimization of Sulfurization Time and Temperature for Fabrication of  $\text{Cu}_2\text{ZnSnS}_4$  (CZTS) Thin Films. *Superlattices Microstruct.* **2019**, *126*, 32–41. [[CrossRef](#)]
122. Xue, Y.; Yu, B.; Li, W.; Feng, S.; Wang, Y.; Huang, S.; Zhang, C.; Qiao, Z. Effect of Annealing Atmosphere on Properties of  $\text{Cu}_2\text{ZnSn}(\text{S,Se})_4$  Thin Films. *Superlattices Microstruct.* **2017**, *112*, 311–317. [[CrossRef](#)]
123. Sharmin, A.; Kumar, K.; Al Mamun, S.M.M.; Hossain, M. Influence of Annealing Conditions on the Performance of Sputtered Grown CZTS Thin Film Solar Cells. *AIP Adv.* **2022**, *12*, 115025. [[CrossRef](#)]
124. Wei, Y.; Zhou, K.; Meng, X.; Sun, X.; Ma, Z.; Li, Z.; Zhuang, D. Improving the Performance of Solution-Based CZTSSe Absorber by Selenization Annealing with Selenium Powder in Argon. *J. Alloys Compd.* **2024**, *976*, 173123. [[CrossRef](#)]
125. Bodeux, R.; Mollica, F.; Delbos, S. Growth of  $\text{Cu}_2\text{ZnSnSe}_4$  by Cosputtering and Reactive Annealing Atmosphere. *Sol. Energy Mater. Sol. Cells* **2015**, *132*, 67–73. [[CrossRef](#)]
126. Li, W.; Han, X.; Zhao, Y.; Liu, L.; Wang, J.; Yang, S.; Tanaka, T.  $\text{Cu}_2\text{ZnSnS}_4$  Alloys Synthesized from  $\text{Cu}_2\text{SnS}_3$ @ZnS Nanoparticles via a Facile Hydrothermal Approach. *Mater. Lett.* **2014**, *125*, 167–170. [[CrossRef](#)]
127. Nagamalleswari, D.; Kumar, Y.K.; Kiran, Y.B.; Babu, G.S. Preparation and Characterization of  $\text{Cu}_2\text{ZnSnS}_4$  Thin Films by Two-Stage Process. *Energy Sources Part A Recovery Util. Environ. Eff.* **2019**, *41*, 3001–3012. [[CrossRef](#)]
128. Gordillo, G.; Becerra, R.; Calderón, C. Novel Chemical Route for Deposition of  $\text{Cu}_2\text{ZnSnS}_4$  Photovoltaic Absorbers. *J. Braz. Chem. Soc.* **2017**, *29*, 649–658. [[CrossRef](#)]
129. Park, J.; Song, M.; Jung, W.M.; Lee, W.Y.; Kim, H.; Kim, Y.; Hwang, C.; Shim, I.-W. Syntheses of  $\text{Cu}_2\text{SnS}_3$  and  $\text{Cu}_2\text{ZnSnS}_4$  Nanoparticles with Tunable Zn/Sn Ratios under Multibubble Sonoluminescence Conditions. *Dalton Trans.* **2013**, *42*, 10545. [[CrossRef](#)]

130. Bär, M.; Schubert, B.-A.; Marsen, B.; Krause, S.; Pookpanratana, S.; Unold, T.; Weinhardt, L.; Heske, C.; Schock, H.-W. Impact of KCN Etching on the Chemical and Electronic Surface Structure of  $\text{Cu}_2\text{ZnSnS}_4$  Thin-Film Solar Cell Absorbers. *Appl. Phys. Lett.* **2011**, *99*, 152111. [[CrossRef](#)]
131. Chen, R.; Fan, J.; Li, H.; Liu, C.; Mai, Y. Efficiency Enhancement of  $\text{Cu}_2\text{ZnSnS}_4$  Solar Cells via Surface Treatment Engineering. *R. Soc. Open Sci.* **2018**, *5*, 171163. [[CrossRef](#)] [[PubMed](#)]
132. López-Marino, S.; Sánchez, Y.; Placidi, M.; Fairbrother, A.; Espindola-Rodríguez, M.; Fontané, X.; Izquierdo-Roca, V.; López-García, J.; Calvo-Barrio, L.; Pérez-Rodríguez, A.; et al. ZnSe Etching of Zn-Rich  $\text{Cu}_2\text{ZnSnSe}_4$ : An Oxidation Route for Improved Solar-Cell Efficiency. *Chem. A Eur. J.* **2013**, *19*, 14814–14822. [[CrossRef](#)]
133. Xie, H.; Sánchez, Y.; López-Marino, S.; Espindola-Rodríguez, M.; Neuschitzer, M.; Sylla, D.; Fairbrother, A.; Izquierdo-Roca, V.; Pérez-Rodríguez, A.; Saucedo, E. Impact of Sn(S,Se) Secondary Phases in  $\text{Cu}_2\text{ZnSn(S,Se)}_4$  Solar Cells: A Chemical Route for Their Selective Removal and Absorber Surface Passivation. *ACS Appl. Mater. Interfaces* **2014**, *6*, 12744–12751. [[CrossRef](#)] [[PubMed](#)]
134. Lai, F.-I.; Yang, J.-F.; Li, J.-E.; Hsu, Y.-C.; Kuo, S.-Y. Suppression of  $\text{SnS}_2$  Secondary Phase on  $\text{Cu}_2\text{ZnSnS}_4$  Solar Cells Using Multi-Metallic Stacked Nanolayers. *Nanomaterials* **2023**, *13*, 432. [[CrossRef](#)]
135. Minbashi, M.; Ghobadi, A.; Yazdani, E.; Ahmadkhan Kordbacheh, A.; Hajjiah, A. Efficiency Enhancement of CZTSSe Solar Cells via Screening the Absorber Layer by Examining of Different Possible Defects. *Sci. Rep.* **2020**, *10*, 21813. [[CrossRef](#)]
136. Yussuf, S.T.; Nwambaekwe, K.C.; Ramoroka, M.E.; Iwuoha, E.I. Photovoltaic Efficiencies of Microwave and  $\text{Cu}_2\text{ZnSnS}_4$  (CZTS) Superstrate Solar Cells. *Mater. Today Sustain.* **2023**, *21*, 100287. [[CrossRef](#)]
137. Liu, F.; Huang, J.; Sun, K.; Yan, C.; Shen, Y.; Park, J.; Pu, A.; Zhou, F.; Liu, X.; Stride, J.A.; et al. Beyond 8% Ultrathin Kesterite  $\text{Cu}_2\text{ZnSnS}_4$  Solar Cells by Interface Reaction Route Controlling and Self-Organized Nanopattern at the Back Contact. *NPG Asia Mater.* **2017**, *9*, e401. [[CrossRef](#)]
138. Chawla, V.; Clemens, B. Effect of Composition on High Efficiency CZTSSe Devices Fabricated Using Co-Sputtering of Compound Targets. In Proceedings of the 2012 38th IEEE Photovoltaic Specialists Conference, Austin, TX, USA, 3–8 June 2012; pp. 2990–2992.
139. Zhang, Y.-M.; Jia, Z.-J.; Zhao, Z.-Y. Secondary Phases in  $\text{Cu}_2\text{ZnSnS}_4$  Thin Film Solar Cell: The Role of Interfaces. *Phys. B Condens. Matter* **2022**, *626*, 413539. [[CrossRef](#)]
140. Saha, S. A Status Review on  $\text{Cu}_2\text{ZnSn(S,Se)}_4$ -Based Thin-Film Solar Cells. *Int. J. Photoenergy* **2020**, *2020*, 3036413. [[CrossRef](#)]
141. Zhang, Z.; Yao, L.; Zhang, Y.; Ao, J.; Bi, J.; Gao, S.; Gao, Q.; Jeng, M.-J.; Sun, G.; Zhou, Z.; et al. Modified Back Contact Interface of CZTSe Thin Film Solar Cells: Elimination of Double Layer Distribution in Absorber Layer. *Adv. Sci.* **2018**, *5*, 1700645. [[CrossRef](#)] [[PubMed](#)]
142. Redinger, A.; Groiss, H.; Sandler, J.; Djemour, R.; Regesch, D.; Gerthsen, D.; Siebentritt, S. Epitaxial  $\text{Cu}_2\text{ZnSnS}_4$  Thin Films and Devices. *Thin Solid. Films* **2015**, *582*, 193–197. [[CrossRef](#)]
143. Azzouzi, M.; Cabas-Vidani, A.; Haass, S.G.; Röhr, J.A.; Romanyuk, Y.E.; Tiwari, A.N.; Nelson, J. Analysis of the Voltage Losses in CZTSSe Solar Cells of Varying Sn Content. *J. Phys. Chem. Lett.* **2019**, *10*, 2829–2835. [[CrossRef](#)] [[PubMed](#)]
144. Lai, F.; Yang, J.; Hsu, Y.; Kuo, S. Sustainable  $\text{Cu}_2\text{ZnSnSe}_4$  Photovoltaic Cells Fabricated with a Sputtered CdS Buffer Layer. *Progress. Photovolt.* **2020**, *28*, 1012–1023. [[CrossRef](#)]
145. Ahmed, S.; Reuter, K.B.; Gunawan, O.; Guo, L.; Romankiw, L.T.; Deligianni, H. A High Efficiency Electrodeposited  $\text{Cu}_2\text{ZnSnS}_4$  Solar Cell. *Adv. Energy Mater.* **2012**, *2*, 253–259. [[CrossRef](#)]
146. Yao, L.; Ao, J.; Jeng, M.-J.; Bi, J.; Gao, S.; Sun, G.; He, Q.; Zhou, Z.; Sun, Y.; Chang, L.-B. A CZTSe Solar Cell with 8.2% Power Conversion Efficiency Fabricated Using Electrodeposited Cu/Sn/Zn Precursor and a Three-Step Selenization Process at Low Se Pressure. *Sol. Energy Mater. Sol. Cells* **2017**, *159*, 318–324. [[CrossRef](#)]
147. Sun, K.; Yan, C.; Liu, F.; Hao, X. Towards 9% Sulfide CZTS Solar Cells Fabricated by a Sol-Gel Process. In Proceedings of the 2018 IEEE 7th World Conference on Photovoltaic Energy Conversion (WCPEC) (A Joint Conference of 45th IEEE PVSC, 28th PVSEC & 34th EU PVSEC), Waikoloa, HI, USA, 10–15 June 2018; pp. 856–858.
148. Su, Z.; Sun, K.; Han, Z.; Cui, H.; Liu, F.; Lai, Y.; Li, J.; Hao, X.; Liu, Y.; Green, M.A. Fabrication of  $\text{Cu}_2\text{ZnSnS}_4$  Solar Cells with 5.1% Efficiency via Thermal Decomposition and Reaction Using a Non-Toxic Sol-Gel Route. *J. Mater. Chem. A* **2014**, *2*, 500–509. [[CrossRef](#)]
149. Swami, S.K.; Chaturvedi, N.; Kumar, A.; Chander, N.; Dutta, V.; Kumar, D.K.; Ivaturi, A.; Senthilarasu, S.; Upadhyaya, H.M. Spray Deposited Copper Zinc Tin Sulphide ( $\text{Cu}_2\text{ZnSnS}_4$ ) Film as a Counter Electrode in Dye Sensitized Solar Cells. *Phys. Chem. Chem. Phys.* **2014**, *16*, 23993–23999. [[CrossRef](#)] [[PubMed](#)]
150. Wright, L.D.; Lowe, J.C.; Bliss, M.; Tsai, V.; Togay, M.; Betts, T.R.; Walls, J.M.; Malkov, A.V.; Bowers, J.W. Water Based Spray Pyrolysis of Metal-Oxide Solutions for  $\text{Cu}_2\text{ZnSn(S,Se)}_4$  Solar Cells Using Low Toxicity Amine/Thiol Complexants. *Thin Solid. Films* **2019**, *669*, 588–594. [[CrossRef](#)]
151. Sun, K.; Yan, C.; Liu, F.; Huang, J.; Zhou, F.; Stride, J.A.; Green, M.; Hao, X. Over 9% Efficient Kesterite  $\text{Cu}_2\text{ZnSnS}_4$  Solar Cell Fabricated by Using  $\text{Zn}_{1-x}\text{Cd}_x\text{S}$  Buffer Layer. *Adv. Energy Mater.* **2016**, *6*, 1600046. [[CrossRef](#)]
152. Tampo, H.; Kim, S.; Nagai, T.; Shibata, H.; Niki, S. Improving the Open Circuit Voltage through Surface Oxygen Plasma Treatment and 11.7% Efficient  $\text{Cu}_2\text{ZnSnSe}_4$  Solar Cell. *ACS Appl. Mater. Interfaces* **2019**, *11*, 13319–13325. [[CrossRef](#)]
153. Shin, B.; Zhu, Y.; Bojarczuk, N.A.; Jay Chey, S.; Guha, S. Control of an Interfacial  $\text{MoSe}_2$  Layer in  $\text{Cu}_2\text{ZnSnSe}_4$  Thin Film Solar Cells: 8.9% Power Conversion Efficiency with a TiN Diffusion Barrier. *Appl. Phys. Lett.* **2012**, *101*, 053903. [[CrossRef](#)]
154. Hu, J.-G.; Wu, T.; Ishaq, M.; Farooq, U.; Chen, S.; Zheng, Z.-H.; Su, Z.-H.; Lin, X.-D.; Fan, P.; Ma, H.-L.; et al. Pulsed Laser Deposited and Sulfurized  $\text{Cu}_2\text{ZnSnS}_4$  Thin Film for Efficient Solar Cell. *Sol. Energy Mater. Sol. Cells* **2021**, *233*, 111383. [[CrossRef](#)]

155. Li, J.; Huang, Y.; Huang, J.; Liang, G.; Zhang, Y.; Rey, G.; Guo, F.; Su, Z.; Zhu, H.; Cai, L.; et al. Defect Control for 12.5% Efficiency  $\text{Cu}_2\text{ZnSnSe}_4$  Kesterite Thin-Film Solar Cells by Engineering of Local Chemical Environment. *Adv. Mater.* **2020**, *32*, 2005268. [[CrossRef](#)] [[PubMed](#)]
156. Taskesen, T.; Neerken, J.; Schoneberg, J.; Pareek, D.; Steininger, V.; Parisi, J.; Gütay, L. Device Characteristics of an 11.4% CZTSe Solar Cell Fabricated from Sputtered Precursors. *Adv. Energy Mater.* **2018**, *8*, 1703295. [[CrossRef](#)]
157. Yan, C.; Huang, J.; Sun, K.; Johnston, S.; Zhang, Y.; Sun, H.; Pu, A.; He, M.; Liu, F.; Eder, K.; et al.  $\text{Cu}_2\text{ZnSnS}_4$  Solar Cells with over 10% Power Conversion Efficiency Enabled by Heterojunction Heat Treatment. *Nat. Energy* **2018**, *3*, 764–772. [[CrossRef](#)]
158. Larsen, J.K.; Larsson, F.; Törndahl, T.; Saini, N.; Riekehr, L.; Ren, Y.; Biswal, A.; Hauschild, D.; Weinhardt, L.; Heske, C.; et al. Cadmium Free  $\text{Cu}_2\text{ZnSnS}_4$  Solar Cells with 9.7% Efficiency. *Adv. Energy Mater.* **2019**, *9*, 1900439. [[CrossRef](#)]
159. Gong, Y.; Zhu, Q.; Li, B.; Wang, S.; Duan, B.; Lou, L.; Xiang, C.; Jedlicka, E.; Giridharagopal, R.; Zhou, Y.; et al. Elemental De-Mixing-Induced Epitaxial Kesterite/CdS Interface Enabling 13%-Efficiency Kesterite Solar Cells | Nature Energy. *Nat. Energy* **2022**, *7*, 966–977. [[CrossRef](#)]
160. Nguyen, T.H.; Septina, W.; Fujikawa, S.; Jiang, F.; Harada, T.; Ikeda, S.  $\text{Cu}_2\text{ZnSnS}_4$  Thin Film Solar Cells with 5.8% of Conversion Efficiency Obtained by a Facile Spray Pyrolysis Technique. *RSC Adv.* **2015**, *5*, 77565–77571. [[CrossRef](#)]

**Disclaimer/Publisher's Note:** The statements, opinions and data contained in all publications are solely those of the individual author(s) and contributor(s) and not of MDPI and/or the editor(s). MDPI and/or the editor(s) disclaim responsibility for any injury to people or property resulting from any ideas, methods, instructions or products referred to in the content.